Department of Applied Physics

Adiabatic control in circuit quantum electrodynamics

Antti Vepsäläinen

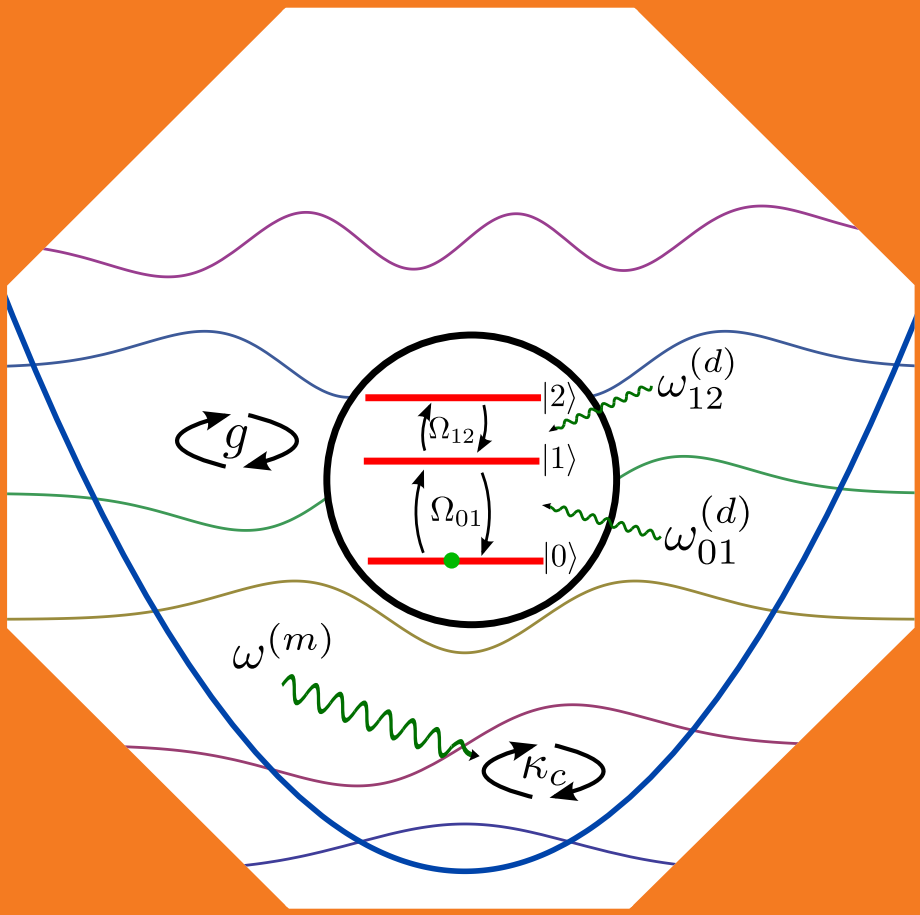

Aalto University

DOCTORAL DISSERTATIONS

Aalto University publication series
DOCTORAL DISSERTATIONS 84/2018

Adiabatic control in circuit quantum electrodynamics

Antti Vepsäläinen

A doctoral dissertation completed for the degree of Doctor of Science (Technology) to be defended, with the permission of the Aalto University School of Science, at a public examination held at the lecture hall T2 of the school on 25 May 2018 at 12.

Aalto University
School of Science
Department of Applied Physics
Kvantti group

Supervising professor
Prof. Jukka Pekola

Thesis advisor
Doc. Sorin Paraoanu

Preliminary examiners
Dr. Lucas Lamata, University of the Basque Country, Spain
Prof. Esa Räsänen, Tampere University of Technology, Finland

Opponent
Prof. David DiVincenzo, RWTH Aachen University, Germany

Aalto University publication series
DOCTORAL DISSERTATIONS 84/2018

ISBN 978-952-60-7975-2 (printed)
ISBN 978-952-60-7976-9 (pdf)
ISSN-L 1799-4934
ISSN 1799-4934 (printed)
ISSN 1799-4942 (pdf)
http://urn.fi/URN:ISBN:978-952-60-7976-9

Unigrafia Oy
Helsinki 2018

Finland

441 697
Printed matter

Aalto University

Abstract

Aalto University, P.O. Box 11000, FI-00076 Aalto www.aalto.fi

Author
Antti Vepsäläinen

Name of the doctoral dissertation
Adiabatic control in circuit quantum electrodynamics

Publisher School of Science

Unit Department of Applied Physics

Series Aalto University publication series DOCTORAL DISSERTATIONS 84/2018

Field of research Engineering physics

Manuscript submitted 20 April 2018 **Date of the defence** 25 May 2018

Permission to publish granted (date) 9 April 2018 **Language** English

☐ **Monograph** ☒ **Article dissertation** ☐ **Essay dissertation**

Abstract

In circuit quantum electrodynamics the coherence of Cooper pairs in superconductors is employed to create macroscopic electric circuits with quantized energy levels. Such circuits can be coupled with each other and exploited as building blocks of a quantum computer. Accurate and robust control of the quantum state in the circuits is a central condition for the operation of the quantum computer and one of the prerequisites for the implementation of complex algorithms used in quantum information processing, such as quantum error correction. In this thesis adiabatic control in circuit quantum electrodynamics is investigated with the focus on manipulating three-level systems.

In adiabatic control the eigenstates of the system are slowly modified by changing the external control parameters, which govern the evolution of the system. If the changes in the parameters are slow enough, the state of the system follows the eigenstates in the adiabatic basis, thereby realizing the intended operation. The advantage of adiabatic control is its inherent robustness to small errors or noise in the control parameters; the result of the state manipulation only depends on the asymptotic values of the control parameters, but not on their exact values during the process.

Shortcuts to adiabaticity can be used to speed up the otherwise slow adiabatic control by introducing a correction pulse that compensates the diabatic losses during the state manipulation. This allows one to overcome the limitation on the speed of the protocol but simultaneously reduces the method's robustness to the variations in the control parameters. If the level of noise in the control parameters is known, using the shortcut it is possible to find the optimal level of robustness which is required to mitigate the noise.

Circuit quantum electrodynamics offers a perfect experimental platform for investigating quantum control due to the possibility of realizing complicated control schemes using microwave electronics. With commercially available digital-to-analog converters the control signals can be digitally created, which enables accurate and coherent control of the quantum circuit.

In this thesis both theoretical and experimental results on adiabatic control applied to superconducting transmon circuits are presented. It is shown that stimulated Raman adiabatic passage can be used for population transfer in a three-level transmon, which can be further improved using shortcuts to adiabaticity. Furthermore, a scheme for implementing robust superadiabatic rotation gates in transmon is proposed. Finally, it is demonstrated that superconducting qubit can be used as an ultra-sensitive detector of magnetic flux.

Keywords Adiabatic control, superadiabatic control, circuit QED, STIRAP, quantum metrology

ISBN (printed) 978-952-60-7975-2	**ISBN (pdf)** 978-952-60-7976-9	
ISSN-L 1799-4934	**ISSN (printed)** 1799-4934	**ISSN (pdf)** 1799-4942
Location of publisher Helsinki	**Location of printing** Helsinki	**Year** 2018
Pages 150	**urn** http://urn.fi/URN:ISBN:978-952-60-7976-9	

Tekijä
Antti Vepsäläinen

Väitöskirjan nimi
Adiabaattinen hallinta piirikvanttisähködynamiikassa

Julkaisija Perustieteiden korkeakoulu

Yksikkö Teknillisen fysiikan laitos

Sarja Aalto University publication series DOCTORAL DISSERTATIONS 84/2018

Tutkimusala Teknillinen fysiikka

Käsikirjoituksen pvm 20.04.2018 **Väitöspäivä** 25.05.2018

Julkaisuluvan myöntämispäivä 09.04.2018 **Kieli** Englanti

☐ **Monografia** ☒ **Artikkeliväitöskirja** ☐ **Esseeväitöskirja**

Tiivistelmä

Piirikvanttisähködynamiikassa suprajohteissa esiintyvien Cooperin parien koherenttiuden avulla luodaan makroskooppisia sähköpiirejä, joiden energiatilat ovat kvantittuneet. Näitä piirejä voidaan kytkeä toisiinsa ja käyttää kvanttitietokoneen rakennuspalikoina. Piirien kvanttitilan tarkka ja luotettava hallinta on edellytys kvanttitietokoneen toiminalle sekä kvantti-informaation käsittelyssä tarvittavien monimutkaisten algoritmien toteuttamiselle.

Tässä väitöskirjassa tutkitaan kvanttipiirien adiabaattista hallintaa keskittyen kolmitasosysteemeihin. Adiabaattisessa hallinnassa systeemin ominaistiloja muokataan muuttamalla hitaasti ulkoisia ohjausparametreja. Mikäli muutokset parametreissä ovat tarpeeksi hitaita, systeemin tila seuraa sen adiabaattisia ominaistiloja, joiden kehittyminen tuottaa tavoitellun lopputilan. Adiabaattisen hallinnan etuja ovat luontainen kestävyys ohjaussignaalien pieniä virheitä ja häiriöitä vastaan. Lopullinen kvanttitila riippuukin lähinnä ohjaussignaalien asymptoottisista arvoista niiden tilan kehityksen aikaisten tarkkojen arvojen sijaan.

Adiabaattiset prosessit ovat yleensä hitaita, mutta tilan kehitykseen on olemassa myös nopeampia oikopolkuja. Adiabaattinen oikopolku luodaan lisäämällä systeemiin tarkkaan muotoiltu ohjaussignaali, joka kumoaa tilan nopeasta kehityksestä johtuvat virheet. Oikopolku poistaa rajoitukset tilan kehitysnopeudelle, mutta lopputilan herkkyys ohjaussignaalien virheille kasvaa samassa suhteessa. Mikäli ohjaussignaalien häiriötaso on tiedossa, adiabaattista oikopolkua käyttäen voidaan löytää ihanteellinen tasapaino hallinnan nopeuden ja virheenkestävyyden välillä.

Piirikvanttisähködynamiikka tarjoaa erinomaisen kokeellisen ympäristön kvanttitilojen hallinnan tutkimiseen, sillä mikroaaltoelektroniikkaa käyttäen voidaan luoda monimutkaisia ohjaussignaaleja. Ohjaussignaalit voidaan tuottaa digitaalisesti kaupallisesti saatavilla olevilla digitaali-analogimuuntimilla, mikä mahdollistaa tarkkojen ja keskenään koherenttien ohjaussignaalien luomisen.

Tässä väitöskirjassa esitetään sekä teoreettisia että kokeellisia tuloksia suprajohtavien transmonpiirien tilan hallinnasta. Työssä osoitetaan, että stimuloitua adiabaattista Raman-ohitusta voidaan käyttää perustilalla olevan kolmitasopiirin virittämiseen toiselle viritystilalleen ja että tämän onnistumista voidaan parantaa käyttäen adiabaattista oikopolkua. Työssä myös esitellään menetelmä nopeiden adiabaattisten kiertoporttien toteuttamiseksi. Lopuksi näytetään kuinka suprajohtavaa kaksitasosysteemiä voidaan käyttää äärimmäisen herkkänä magneettikentän ilmaisimena.

Avainsanat Adiabaattinen hallinta, superadiabaattinen hallinta, piirikvanttisähködynamiikka, STIRAP, kvanttimetrologia

ISBN (painettu) 978-952-60-7975-2 **ISBN (pdf)** 978-952-60-7976-9

ISSN-L 1799-4934 **ISSN (painettu)** 1799-4934 **ISSN (pdf)** 1799-4942

Julkaisupaikka Helsinki **Painopaikka** Helsinki **Vuosi** 2018

Sivumäärä 150 **urn** http://urn.fi/URN:ISBN:978-952-60-7976-9

Preface

Most of all I would like to thank my instructor Dr. Sorin Paraoanu, who has been guiding me since I came to the Low temperature laboratory as a second year student. He has introduced me to numerous interesting problems, some of which have ended up as parts of this thesis. I would also like to thank my supervisor Prof. Jukka Pekola who, though not directly contributing to my research, has made sure that my work advances on time.

There have been many people who have helped me with my work during my years in the laboratory. I am indebted to the former members of Kvantti group, Dr. Khartikeyan Sampath Kumar, who first introduced me into the world of quantum experiments and Dr. Khattiya Chalapat who guided me into the peculiarities of microwaves. I am especially thankful to Sergey Danilin who started his doctoral studies at the same time as I. Most of the experimental work in the thesis is done in collaboration with him, which has been both efficient and pleasant. I thank Dr. Dong Lan for sharing his experience in circuit quantum electrodynamics. Prof. Giuseppe Falci I thank for interesting discussions on STIRAP.

The daily coffee breaks have been an important part of the social life in the laboratory. In addition to providing relaxation during the working days, the coffee table has constantly been an arena of fierce scientific arguments, topics of which have ranged from biology to quantum field theories. I would like to thank Jere Mäkinen, Dr. Samuli Autti, Dr. Niklas Hietala, Dr. Petri Heikkinen, Dr. Juho Rysti, Dr. Jaakko Nissinen, Jukka-Pekka Kaikkonen and Timo Kamppinen for their contributions to the discussions. Daniel Cox, Dr. Ville Kauppila, Jorge Santos and Dr. Vladislav Zavyalov I would like to thank for organizing and participating in the weekly sauna evenings that have never lacked beer or delicious snacks. To Sampo Hämäläinen and Dr. Tuomas Mutanen I am thankful for their

company during the lunch breaks.

Finally I would like to express my gratitude to my mother Outi, father Pekka and sister Kaisa for their support and interest in my work. My deepest thanks to my beloved partner Armi for always cheering me up and trying to convince me that this thesis will some day be finished.

Espoo, April 25, 2018,

Antti Vepsäläinen

Contents

List of Publications

This thesis consists of an overview and of the following publications which are referred to in the text by their Roman numerals.

I A. Vepsäläinen, S. Danilin, and G. S. Paraoanu. Optimal superadiabatic population transfer and gates by dynamical phase corrections. *Quantum Science and Technology*, 3(2), 24006, 2018.

II S. Danilin, A. V. Lebedev, A. Vepsäläinen, G. B. Lesovik, G. Blatter, G. S. Paraoanu. Quantum-enhanced magnetometry by phase-estimation algorithms with a single artificial atom. Accepted for publication in *npj Quantum Information*, 2018.

III A. Vepsäläinen, S. Danilin, and G. S. Paraoanu. Superadiabatic population transfer by loop driving in a superconducting circuit. Submitted to *Phys. Rev. Lett.*, 2017.

IV A. Vepsäläinen and G. S. Paraoanu. Cross-coupling effects in circuit-QED stimulated Raman adiabatic passage. In *proceedings of 28th International Conference on Low Temperature Physics, J. Phys.: Conf. Ser.*, 969(1), 012141, 2018.

V A. Vepsäläinen, S. Danilin, E. Paladino, G. Falci, and G. S. Paraoanu. Quantum Control in Qutrit Systems Using Hybrid Rabi-STIRAP Pulses. *Photonics*, 3(4), 62, 2016.

VI K. S. Kumar, A. Vepsäläinen, S. Danilin, and G. S. Paraoanu. Stimulated Raman adiabatic passage using a three-level superconducting circuit. *Nature Communications*, 7, 10628, 2016.

Author's Contribution

Publication I: "Optimal superadiabatic population transfer and gates by dynamical phase corrections"

The author performed the calculations and simulations for the article and wrote the draft of the paper.

Publication II: "Quantum-enhanced magnetometry by phase-estimation algorithms with a single artificial atom"

The author contributed to the experimental setup and participated in the measurements.

Publication III: "Superadiabatic population transfer by loop driving in a superconducting circuit"

The author had a key contribution in the measurements, made the simulations and calculations for the article, and wrote the manuscript together with the other authors.

Publication IV: "Cross-coupling effects in circuit-QED stimulated Raman adiabatic passage"

The author did the calculations and wrote the manuscript.

Publication V: "Quantum Control in Qutrit Systems Using Hybrid Rabi-STIRAP Pulses"

The author derived some of the analytical results, made the simulations and contributed to the writing of the paper.

Publication VI: "Stimulated Raman adiabatic passage using a three-level superconducting circuit"

The author significantly contributed to the experiments, analyzed the data, made the simulations and wrote the draft of the manuscript.

Other publications by the author

[1] S. Danilin, A. Vepsäläinen, and G. S. Paraoanu. Experimental state control by fast non-Abelian holonomic gates with a superconducting qutrit. *Physica Scripta.*, 93, 055101, 2018.

[2] I. Pietikäinen , S. Danilin, K. S. Kumar, A. Vepsäläinen, D. S. Golubev, J. Tuorila, and G. S. Paraoanu. Observation of the Bloch-Siegert shift in a driven quantum-to-classical transition. *Physical Review B*, 96(2), 020501, 2017.

[3] M. Silveri, K. S. Kumar, J. Tuorila, J. Li, A. Vepsäläinen, E. V. Thuneberg, and G. S. Paraoanu. Stückelberg interference in a superconducting qubit under periodic latching modulation. *New Journal of Physics*, 17(4), 043058, 2015.

[4] J. Li, M. P. Silveri, K. S. Kumar, J-M. Pirkkalainen, A. Vepsäläinen, W. C. Chien,and G. S. Paraoanu. Motional averaging in a superconducting qubit. *Nature Communications*, 4, 1-6.,1420, 2013.

[5] A. Vepsäläinen, K. Chalapat, and G. S. Paraoanu. Measuring the microwave magnetic permeability of small samples using the short-circuit transmission line method. *IEEE Transactions on Instrumentation and Measurement* 62(9), 2503-2510, 2013.

1. Introduction

The idea of using quantum mechanics to speed up computations first came up in the 1970s with several theoretical proposals [1, 2] followed by Richard Feynman's famous result that quantum mechanics can only be effectively simulated using a quantum computer [3]. An important step was taken by David Deutsch who managed to define the model of a universal quantum computer [4] thereby formalizing the concept of quantum information processing. That led to the invention of the first quantum algorithms, which can be used solve a computational problem faster than any known classical algorithm [5, 6, 7]. The discovery has stimulated increasing experimental efforts to realize devices of growing complexity that are able to perform the quantum algorithms or simulate quantum physics [8]. An essential initial step in the effort is to be able to coherently control a single quantum system, which was first achieved in the 1970s [9, 10].

Nowadays accurately controllable quantum systems can be realized in several different experimental platforms such as quantum optics [11], nitrogen vacancies in diamonds [12], trapped ions [13], ultracold atomic gases [14], or quantum dots in silicon [15]. Even though in all of these fields there has been significant progress during the last decade, perhaps the most prominent platform for realizing a quantum computer is circuit quantum electrodynamics (QED) [16, 17] which employs superconducting electric circuits operated as macroscopic artificial atoms. The circuits retain their quantum nature despite their large size due to the collective behaviour of Cooper pairs in superconductors. Consequently, many of the properties of the circuit *e.g.* energy spectrum, do not depend on the microscopic material parameters, but rather can be controlled by tuning the macroscopic parameters of the electric circuit such as capacitance and inductance, rendering the technology versatile and flexible. In addition, the technology holds the promise of scalability due to the sophisticated fabri-

cation methods which can be inherited from the semiconductor industry.

Despite the recent advantages in controlling the superconducting circuits and isolating them from the harmful influence of their environment, the work is not yet done. In order to reach the threshold for quantum error correction [18, 19], the coherence times of the quantum circuits have to increase even further. This far there has been exponential improvement with time [20] which gives hope that the evolution of the technology still continues fast.

However, long coherence times alone are not enough for satisfying the requirements of quantum computing [8]; mistakes in the external signals used to manipulate the state of the system also lead to incorrect operations, which result in increased error rates. Therefore it is essential to develop control methods that are insensitive to fluctuations in the control parameters. The main part of the work presented in this thesis is dedicated to investigating such methods and applying them to circuit quantum electrodynamics.

The thesis is organized as follows: the basics of circuit QED are reviewed in chapter 2. In chapter 3 it is described how adiabatic manipulation can be used to control a three-level system. There the focus is on stimulated Raman adiabatic passage (STIRAP) method, which is experimentally demonstrated in Publication VI. Publication V theoretically investigates the combination of STIRAP with a Rabi pulse, which allows for creation of an arbitrary three state superpositions. In Publication IV the reduction of the STIRAP fidelity due to small anharmonicity of the transmon circuit is studied and optimal drive parameters are found in the presence of decoherence.

In Chapter 4 it is shown that adiabatic evolution can be made faster using shortcuts to adiabaticity (STA). In Publication III we have experimentally implemented the superadiabatic STIRAP (saSTIRAP) protocol, which employs a shortcut that allows the system to follow its adiabatic state even though the adiabatic condition is broken. In Publication I we have further studied saSTIRAP and shown that it is possible to create a robust NOT-gate between the ground state and the second excited state of the system.

Superconducting quantum interference devices can be used as ultrasensitive detectors of magnetic fields. In Chapter 5 it is shown that the coherence of the transmon qubit can be used to improve the resolution of phase detection, which can be linked to magnetic flux, thereby realizing

a detector which accuracy is only limited by the Heisenberg uncertainty principle. The experiment is presented in Publication II.

In Chapter 6 the experimental system is described and the numerical methods applied in simulating the time evolution of the transmon are shortly presented. Finally, the results discussed in the thesis are concluded in Chapter 7.

2. Circuit quantum electrodynamics

Circuit quantum electrodynamics (QED) [21] is an extension of cavity quantum electrodynamics (cQED) [22, 23, 24] which studies the interaction between atoms and light confined in an optical cavity. In the context of QED, the distinctive feature of atoms is their rich electronic energy-level structure, which is discrete and strongly anharmonic. Due to the anharmonicity it is possible to excite the electrons separately by shining the atom with a laser which wavelength matches only the target transition. The excited atom is protected from the spontaneous emission by the off-resonant cavity, which suppresses the vacuum modes to which the excitation could decay [22]. This makes it possible to maintain the coherence of the atomic state long enough to control and readout the quantum states of individual atoms. This is a powerful concept, which enables probing the fundamental laws of quantum mechanics. However, observing the joint evolution of multiple atoms is a challenge, because it is hard to keep them in place and couple to each other reliably. In circuit QED the elements have macroscopic size, eliminating such problems.

The circuit analog of an optical cavity is a microwave resonator, which could be realized with lumped element capacitors and inductors at low frequencies. In the frequency range of 3 - 10 GHz, which is relevant to the circuit QED, the coplanar microwave resonators are fabricated as transmission lines that are isolated from the input and output lines with gaps that create impedance mismatch in the line. The artificial atoms used to replace the real atoms of cQED are based on Josephson junctions [25] which add non-linear voltage-current characteristics to the circuit. In principle the non-linearity required for discrete quantum control could be achieved with diodes or any other non-linear element, but Josephson junctions have a very special feature of being dissipationless. Josephson junctions connect two superconductors with a small gap filled with

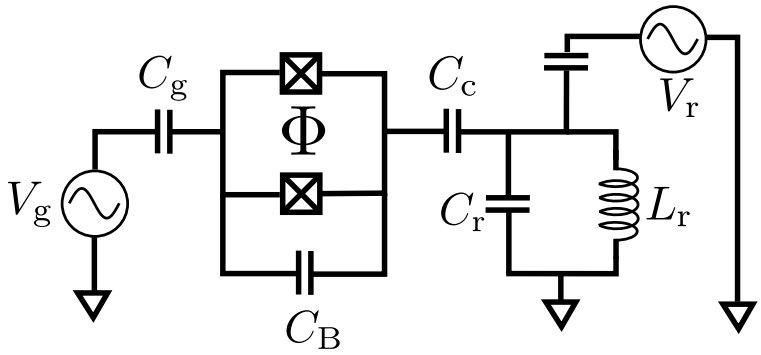

Figure 2.1. Simplified block diagram of a transmon. The transmon is coupled to a gate line with gate capacitance C_g and to a microwave resonator with the capacitance C_c. C_B is the internal transmon capacitance and C_r and L_r are the capacitance and the inductance of the resonator. V_g is the gate voltage and V_r is the voltage used to probe the resonator. The external magnetic flux Φ pierces the transmon loop.

inductive material, through which the Cooper pairs can coherently tunnel. From combinations of capacitors, inductors and Josephson junctions it is possible to create electric circuits in which different variables are quantized such as the charge [17], the flux [26, 27], or the superconducting phase difference [28, 29]. The quantization of the circuit parameters leads to discrete energy levels, which can be employed for quantum control. All the designs have their strengths and weaknesses, but in this work I concentrate on one flavor of charge qubits called transmon [30], which is designed to be very insensitive to noise caused by the charge fluctuations. This allows for long coherence times and accurate control of the quantum state.

The transmon is a type of a Cooper pair box, which consists of a superconducting island isolated by a Josephson junction, which is connected to the gate electrode via a shunting capacitor, shown in Fig. 2.1. In this simplified picture, the Hamiltonian of the transmon is given by [31]

$$\hat{H}_\mathrm{cpb} = 4E_c \left(\hat{n} - \frac{C_g V_g}{2e} \right)^2 - E_J \cos\hat{\theta}, \tag{2.1}$$

where V_g is the gate voltage applied to the transmon, C_g is the gate capacitance, $\hat{n}$ is the operator for the number of Cooper pairs in the superconducting island, E_J is the Josephson energy of the junction, and $\hat{\theta}$ is the operator for the difference of the superconducting phase at the either sides of the junction. The charging energy $E_\mathrm{C} = e^2/(2C_\Sigma)$ is the combined energy of the gate capacitor C_g, the coupling capacitor C_c, the Josephson junction

capacitance C_q, and an additional capacitor parallel with the junctions C_B such that $C_\Sigma = C_\mathrm{q}+C_\mathrm{c}+C_\mathrm{g}+C_\mathrm{B}$. The first term is analogous to the kinetic energy of the excess Cooper pairs in the superconducting island, whereas the second term can be considered as the potential energy resulting from the change of the phase of the Cooper pairs over the Josephson junction. The eigenstates of the above Hamiltonian can be analytically solved in terms of Mathieu functions [30] $E_m(n_\mathrm{g}) = E_\mathrm{C} a_{2[n_\mathrm{g}]+k(m,n_\mathrm{g})}(-E_\mathrm{J}/(2E_\mathrm{C}))$, where $a_{2[n_\mathrm{g}+k(m,n_\mathrm{g})]}$ is the Mathieu's characteristic value [32]. The solutions only depend on the ratio of the Josephson and the charging energies and the gate charge $n_\mathrm{g} = C_\mathrm{g}V_\mathrm{g}/2$, which are shown in Fig. 2.2 for two different ratios of $E_\mathrm{J}/E_\mathrm{C}$. From there it is apparent that by increasing $E_\mathrm{J}/E_\mathrm{C}$ the energy-levels of the system become insensitive to the gate charge, but the anharmonicity $\Delta = E_1 - E_0 - (E_2 - E_1)$ is simultaneously reduced. Experimentally, the capacitance C_B can be used to reduce E_C, allowing the realization of different ratios of $E_\mathrm{J}/E_\mathrm{C}$, which is essential for eliminating the noise caused by the fluctuating gate charges. The sensitivity of the system to the charge noise can be characterized by the charge dispersion which for 0–1 transition is $\epsilon_\mathrm{g} = \frac{\partial E_{01}}{\partial n_\mathrm{g}}$. In the limit of large $E_\mathrm{J}/E_\mathrm{C}$ the eigenenergies E_m can be evaluated approximately by expanding the cosine term in Eq. (2.1) up to 4:th order and writing the Hamiltonian in the form of a Duffing oscillator [33]

$$\begin{aligned} H_\mathrm{cpb} \approx & 4E_c\left(\hat{n} - \frac{C_g V_g}{2e}\right)^2 - E_\mathrm{J}\left(1 - \frac{\hat{\theta}^2}{2} + \frac{\hat{\theta}^4}{24}\right) \\ = & \sqrt{8E_\mathrm{C}E_\mathrm{J}}(\hat{b}^\dagger\hat{b} + 1/2) - E_\mathrm{J} - E_\mathrm{C}\frac{\left(\hat{b}+\hat{b}^\dagger\right)^4}{12}, \end{aligned} \tag{2.2}$$

where $\hat{b} = \sqrt[4]{8E_\mathrm{C}E_\mathrm{J}}\left(\frac{\hat{\theta}}{\sqrt{16E_\mathrm{C}}} - \frac{i\hat{n}}{\sqrt{2E_\mathrm{J}}}\right)$ and $\frac{C_\mathrm{g}V_\mathrm{g}}{2e}$ is removed using a gauge transformation [30]. The eigenenergies of the perturbed oscillator can be evaluated from the first order perturbation theory as $E_m \approx E_m^{(0)} + E_m^{(1)}$, where $E_m^{(0)}$ are the eigenenergies of the unperturbed harmonic oscillator and $E_m^{(1)} = -\frac{E_\mathrm{C}}{12}\langle m|(\hat{b}+\hat{b}^\dagger)^4|m\rangle$, yielding

$$E_m \approx -E_\mathrm{J} + \sqrt{8E_\mathrm{C}E_\mathrm{J}}\left(m + \frac{1}{2}\right) - \frac{E_\mathrm{C}}{12}(6m^2 + 6m + 3). \tag{2.3}$$

This leads to anharmonicity $\alpha = E_{m+1} - E_m - (E_{m+2} - E_{m+1}) = E_\mathrm{C}$, which is independent of m. Furthermore, from the analytic solution $E_m(n_\mathrm{g})$ in the limit of large $E_\mathrm{J}/E_\mathrm{C}$, the maximum of the differential charge dispersion

$$\max(\epsilon_\mathrm{g}) = -512E_\mathrm{C}\sqrt{\frac{2}{\pi}}\left(\frac{E_\mathrm{J}}{2E_\mathrm{C}}\right)^{7/4}\mathrm{e}^{-\sqrt{8E_\mathrm{J}/E_\mathrm{C}}} \tag{2.4}$$

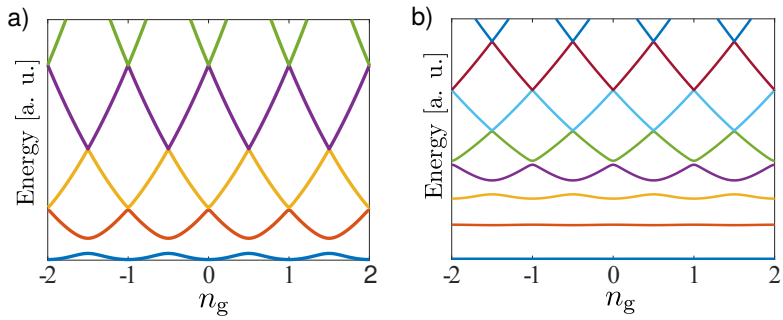

Figure 2.2. The energy level diagram of a Cooper pair box (CPB) as a function of n_g with a) E_J/E_c = 1, and b) E_J/E_C = 10.

can be found to reduce exponentially with E_J/E_C [30, 34]. This implies that it is possible to simultaneously suppress the charge noise and to retain enough anharmonicity to address each of the transitions separately. By using a large capacitor C_B it is possible to fabricate a sample with E_C of several hundreds of MHz while maintaining the ratio of E_J and E_C over 50.

By adding an additional Josephson junction to the circuit it is possible to create a superconducting loop, which makes the transition energies of the circuit sensitive to the magnetic flux penetrating the loop. This allows the tuning of the transition energies during the operation of the circuit, adding an additional tool to control the system.

The Hamiltonian of the two Josephson junctions is given by

$$\hat{H}_J = E_{J_1} \cos\hat{\theta}_1 + E_{J_2} \cos\hat{\theta}_2, \tag{2.5}$$

where E_{J1} and E_{J2} are the Josephson energies of the junctions and $\hat{\theta}_1$ and $\hat{\theta}_2$ are the superconducting phase differences over them. From the quantization of the flux it follows that $\hat{\theta}_1 - \hat{\theta}_2 = 2\pi n + 2\pi\frac{\Phi}{\Phi_0}$, where Φ_0 is the flux quantum, and through substitution to Eq. (2.5), the Hamiltonian can be written

$$\hat{H}_J = -E_{J\Sigma}\left[\cos\left(\frac{\pi\Phi}{\Phi_0}\right)\cos\hat{\varphi} + d\sin\left(\frac{\pi\Phi}{\Phi_0}\right)\sin\hat{\varphi}\right] \tag{2.6}$$

where $E_{J\Sigma} = E_{J1} + E_{J2}$, $d = (E_{J1} - E_{J2})/(E_{J1} + E_{J2})$ is the asymmetry of the junctions and $\hat{\varphi} = (\hat{\theta_1} + \hat{\theta_2})/2$ is the effective phase difference between the superconducting islands. In this configuration the energy levels of the system periodically depend on the flux applied through the loop allowing the tuning of the transition frequencies using an external magnetic field.

2.1 Coupled transmon and resonator

The quantum non-demolition measurement of the transmon state can be realized by capacitively coupling it with a microwave resonator [35]. Due to the coupling, the oscillating voltage in the resonator, $\hat{V} = V_{\mathrm{rms}}(\hat{a}^\dagger + \hat{a})$, instigates the fluctuation of the Cooper pairs in the transmon circuit, resulting in the Hamiltonian

$$\begin{aligned}\hat{H} = &4E_C(\hat{n} - n_g)^2 - E_{J\Sigma}\left[\cos\left(\frac{\pi\Phi}{\Phi_0}\right)\cos\hat{\varphi} + d\sin\left(\frac{\pi\Phi}{\Phi_0}\right)\sin\hat{\varphi}\right] \\ &+ \hbar\omega_r\hat{a}^\dagger\hat{a} + 2c\hat{n}(\hat{a} + \hat{a}^\dagger),\end{aligned} \tag{2.7}$$

where $\omega_r/(2\pi)$ is the resonance frequency of the resonator and the coupling constant

$$c = 2eC_{\mathrm{c}}V_{\mathrm{rms}}/C_\Sigma \tag{2.8}$$

depends on the transmon capacitance and the coupling capacitance C_{c}. As above, the transmon can be considered almost as a harmonic oscillator, in which case the cooper pair number operator can be identified as $\hat{n} = -i\left(\frac{E_{\mathrm{J}}}{8E_{\mathrm{C}}}\right)^{1/4}\frac{1}{\sqrt{2}}(\hat{b} - \hat{b}^\dagger)$, where $\hat{b}$ is the annihilation operator of the transmon. The coupled Hamiltonian can written in the qubit state basis in the form of the Jaynes-Cummings Hamiltonian

$$\hat{H}_{JC} = \hbar\sum_j \omega_j|j\rangle\langle j| + \hbar\omega_r\hat{a}^\dagger\hat{a} + \left(\hbar\sum_i g_{i,i+1}|i\rangle\langle i+1|\hat{a}^\dagger + \mathrm{h.c.}\right), \tag{2.9}$$

where ω_j are the transmon eigenfrequencies and $g_{i,i+1} = c/\hbar\langle i|\hat{n}|j\rangle$. The Jaynes-Cummings Hamiltonian captures the dynamics of the system in a very wide range of parameters, but becomes non-applicable in the limit where the rotating wave approximation is violated such as in the case of ultra-strong coupling [36, 37] or if the coupling of the transmon and the harmonic oscillator cannot be approximated as dipole coupling.

In the dispersive limit, *i.e* when the resonator frequency is far-detuned from the transmon transition frequencies, the resonator can be used to perform a quantum non-demolition measurement of the transmon state. In this case the resonator frequency becomes dependent on the transmon state, which enables one to get information about the transmon by driving the resonator with a measurement tone and measuring the reflected or transmitted photons. In the dispersive limit the Jaynes-Cummings Hamiltonian in Eq. (2.9) can be written as [21, 38]

$$H_{\mathrm{disp}} = \hbar\omega_r\hat{a}^\dagger\hat{a} + \sum_{i=0}^{M}\hbar\omega_i|i\rangle\langle i| + \sum_{i=1}^{M-1}\hbar\chi_{i-1}|i\rangle\langle i| + \sum_{i=0}^{M-1}\hbar s_i|i\rangle\langle i|\hat{a}^\dagger\hat{a}, \tag{2.10}$$

where $\Delta_i = \omega_{i+1} - \omega_i - \omega_\mathrm{r}$, $\chi_i = g_{i,i+1}^2/\Delta_i$ are the dispersive shifts of the single transitions and $s_i = -(\chi_i - \chi_{i-1})$ are the combined shifts. In this picture the transmon state dependent shift in the resonator frequency can be identified in the last term of the Hamiltonian. The experimental realization of the measurement of a three-level transmon state is described in Sec. 6.4.

2.2 Transmon state control

The state of the transmon can be controlled by applying ac voltage to one of the islands of the transmon, which generates the oscillation of the superconducting phase $\hat{\phi}$ due to the ac Josephson effect $\hat{V}(t) = \frac{\partial\hat{\phi}}{\partial t}$. If the driven oscillation is in resonance with the transmon transition frequencies, Rabi oscillations of the transmon state populations take place. The microwave pulses can be sent either through the readout resonator, where they couple to the transmon indirectly through the resonator modes, or using a dedicated gate line, which capacitively couples directly to the transmon. The readout resonator is usually significantly detuned from the transmon and therefore acts as a filter for the driving field. Consequently, the drive amplitude through the resonator has to be quite strong. An additional option is to drive the transmon using the flux line. The oscillation of the flux $\Phi = \Phi_\mathrm{dc} + \Phi_\mathrm{ac}\cos(\omega t)$ through the superconducting loops creates fluctuations in the energy levels of the transmon, as given in Eq. (2.6). In order to suppress the flux noise, the transmon is usually operated in the flux sweep spot, where $\frac{\partial E_{ij}}{\partial\Phi} = 0 \implies \Phi_\mathrm{dc} = 0$. By substituting the time-varying flux into Eq. (2.6) and assuming $\Phi_\mathrm{ac} \ll \Phi_0$ one gets

$$\begin{aligned}
\hat{H}_\mathrm{J} = &- E_{J\Sigma}\Bigg[\cos\left(\frac{\pi\Phi_\mathrm{dc}}{\Phi_0}\right)\cos\left(\frac{\pi\Phi_\mathrm{ac}}{\Phi_0}\cos(\omega t)\right)\cos(\hat{\varphi}) \\
&- \sin\left(\frac{\pi\Phi_\mathrm{dc}}{\Phi_0}\right)\sin\left(\frac{\pi\Phi_\mathrm{ac}}{\Phi_0}\cos(\omega t)\right)\cos(\hat{\varphi}) \\
&+ d\Bigg[\sin\left(\frac{\pi\Phi_\mathrm{dc}}{\Phi_0}\right)\cos\left(\frac{\pi\Phi_\mathrm{ac}}{\Phi_0}\cos(\omega t)\right)\sin(\hat{\varphi}) \\
&+ \cos\left(\frac{\pi\Phi_\mathrm{dc}}{\Phi_0}\right)\sin\left(\frac{\pi\Phi_\mathrm{ac}}{\Phi_0}\cos(\omega t)\right)\sin(\hat{\varphi})\Bigg]\Bigg] \\
\approx &- E_{J\Sigma}\Bigg[\sin\left(\frac{\pi\Phi_\mathrm{dc}}{\Phi_0}\right)\frac{\pi\Phi_\mathrm{ac}}{\Phi_0}\cos(\omega t)\cos(\hat{\varphi}) \\
&+ d\cos\left(\frac{\pi\Phi_\mathrm{dc}}{\Phi_0}\right)\frac{\pi\Phi_\mathrm{ac}}{\Phi_0}\cos(\omega t)\sin(\hat{\varphi})\Bigg] \\
&+ \cos\left(\frac{\pi\Phi_\mathrm{dc}}{\Phi_0}\right)\cos\hat{\varphi} + d\sin\left(\frac{\pi\Phi_\mathrm{dc}}{\Phi_0}\right)\sin\hat{\varphi},
\end{aligned} \tag{2.11}$$

where the time-dependent drive part is

$$\hat{H}_{\mathrm{J}}^{\mathrm{d}} = -E_{J\Sigma} d \sin\left(\frac{\pi\Phi_{\mathrm{dc}}}{\Phi_0}\right) \frac{\pi\Phi_{\mathrm{ac}}}{\Phi_0} \cos(\omega t) \sin(\hat{\varphi}). \tag{2.12}$$

The strength of the flux drive depends on the asymmetry of the junctions and it completely vanishes for identical junctions $d = 0$. The experiments performed in Publication VI are realized using the flux drive, but in the samples used in the later articles the design was abandoned in favour of a dedicated capacitively coupled gate line.

The capacitive coupling of the gate line to the transmon can be modelled as an electromagnetic field, which results in the same kind of a coupling that was derived between the transmon and the resonator in Eq. (2.7). Therefore the capacitive driving can be modelled in the framework of the Jaynes-Cummings Hamiltonian

$$\hat{H}_{\mathrm{JC}}^{\mathrm{d}} = \hat{H}_{\mathrm{JC}} + \hbar \sum_i g_{i,i+1}^{\mathrm{d}} |i\rangle\langle(i+1)| \hat{b}^\dagger \mathrm{e}^{i\omega^{\mathrm{d}} t} + \mathrm{h.c.}, \tag{2.13}$$

where $g_{i,i+1}^{\mathrm{d}}$ is the coupling strength of the driving field to the transmon and ω^{d} is the drive frequency. In the limit of classical driving, where the approximation $\langle \hat{b} \rangle = \langle \hat{b}^\dagger \rangle$ is valid, the driving Hamiltonian can be simplified to

$$\hat{H}_{\mathrm{JC}}^{\mathrm{d}} = \hat{H}_{\mathrm{JC}} + \frac{\hbar}{2} \sum_i \sqrt{i+1}\, \Omega(t) |i\rangle\langle(i+1)| \mathrm{e}^{i(\omega^{\mathrm{d}} t + \phi^{\mathrm{d}})} + \mathrm{h.c.}, \tag{2.14}$$

where $\Omega(t)$ is the effective drive amplitude in units of Rabi frequency and the factor $\sqrt{i+1}$ results from the harmonic approximation of the transmon; similarly to a harmonic oscillator the couplings to the higher transmon levels are stronger. The phase ϕ^{d} is the phase of the driving signal. Usually one only considers the drive terms which are resonant or almost resonant with transmon transition frequencies, but the drives also off-resonantly couple to all the other transitions as described by the above Hamiltonian. Often the off-resonant couplings can be neglected, but there are cases where they play a significant role, which is detrimental to the accurate control of the system as shown in Publication IV.

3. Adiabatic control of a three level system

The adiabatic control of a quantum system is based on slowly changing the external parameters in the Hamiltonian, thereby modifying the eigenstates. If the change in the parameters is slow enough, the system remains in the instantaneous eigenstate of the Hamiltonian. An example of a simpler phenomenon from classical physics would be a ball hanging from a string, held from another end by a person. If the person holding the string moves the string quickly upwards, the ball does not have time to adapt to the changes and stays static initially. After a while it starts to oscillate due to pull of the string. The person can also start pumping the string up and down, providing more energy to the oscillator. On the other hand, if the string is displaced slowly (adiabatically) from one place to another, the ball follows in the end of the string, and if it already was oscillating, the magnitude of the oscillation does not change.

This does not imply that with adiabatic control it would not be possible to excite the system, even though the mechanism is different than with direct Rabi driving. During the adiabatic evolution, the energy of the eigenstate can change due to the modification of the Hamiltonian. Because the changes in the Hamiltonian occur slowly, the system has enough time to adapt to the evolution and therefore stays in the corresponding eigenstate all the time. For example, this is the case in adiabatic passage where the system is forced through an avoided crossing. If the gap in the crossing is large enough, the probability of the diabatic excitations vanishes, as given by the Landau-Zener-Zückelberg formula [39, 40]. Adiabatic control of the system is attractive because the final state of the system does not depend on the exact values of the control parameters during the evolution, but on their asymptotic behaviour. In many cases this enables robust state preparation, which is insensitive to the fluctuations in the control parameters. Such control applied to transmon circuit is studied experimentally

in Publications III and VI and theoretically in Publications I, IV, and V.

Adiabatic theorem can be applied to solving the adiabatic evolution of the system [41]. An estimate of the validity of adiabatic assumption is provided by the adiabatic condition, which plays an essential role in the adiabatic control. In the following the adiabatic equation of motion and the adiabatic condition is derived for Hamiltonians with non-degenerate eigenstates.

The eigenstates $|\psi_n\rangle$ and energies E_n of the system with time-independent Hamiltonian $\hat{H}$ are given by the Schrödinger equation $\hat{H}|\psi_n\rangle = E_n|\psi_n\rangle$. Even if the Hamiltonian were time-dependent, these solutions form an orthonormal basis at any instant of time, though in general the eigenvectors and the energies become time-dependent. Thus any solution to the time-dependent Schrödinger equation can be represented as

$$|\psi(t)\rangle = \sum_n c_n(t)|\psi_n(t)\rangle \mathrm{e}^{-i\theta_n(t)}, \tag{3.1}$$

where $\theta_n(t) = \hbar^{-1}\int_{-\infty}^{t} E_n(t')\mathrm{d}t$ is the accumulated phase of the n:th eigenstate and $|\psi_n(t)\rangle$ are the eigenvectors of the time-independent Schrödinger equation at different time instants. Inserting the state in Eq. (3.1) into the time-dependent Schrödinger equation gives

$$\begin{aligned}
&i\hbar\frac{\partial}{\partial t}|\psi(t)\rangle = \hat{H}|\psi(t)\rangle \qquad\qquad \Longrightarrow \\
&i\hbar\sum_n \big(\dot{c}_n(t)|\psi_n(t)\rangle \mathrm{e}^{-i\theta_n(t)} + c_n(t)|\dot{\psi}_n(t)\rangle \mathrm{e}^{-i\theta_n(t)} + \\
&- ic_n(t)|\psi_n(t)\rangle\dot{\theta}_n(t)\mathrm{e}^{-i\theta_n(t)}\big) = \sum_n c_n(t)\hat{H}|\psi_n(t)\rangle \mathrm{e}^{-i\theta_n(t)} \qquad \Longrightarrow \\
&i\hbar\sum_n (\dot{c}_n(t)|\psi_n(t)\rangle \mathrm{e}^{-i\theta_n(t)} + c_n(t)|\dot{\psi}_n(t)\rangle \mathrm{e}^{-i\theta_n(t)} = 0
\end{aligned} \tag{3.2}$$

where the last term of the l.h.s and the r.h.s cancel each other because $\dot{\theta}_n = \hbar^{-1}E_n(t)$. Solving for the coefficient $\dot{c}_m$ by multiplying the equation with $\langle\psi_m(t)|$ yields

$$\dot{c}_m(t) = -\sum_n c_n\langle\psi_m(t)|\dot{\psi}_n(t)\rangle \mathrm{e}^{-i(\theta_n(t)-\theta_m(t))}. \tag{3.3}$$

The time derivative of the wave function $|\dot{\psi}_n(t)\rangle$ can be simplified by taking the time derivative of the solutions to the time-independent Schrödinger equation in Eq. (3.1) and multiplying them with $\langle\psi_m(t)|$ yielding

$$\langle\psi_m(t)|\dot{\psi}_n(t)\rangle = \frac{\langle\psi_m(t)|\dot{H}|\psi_n(t)\rangle}{E_n(t) - E_m(t)}, \text{ for } n \neq m. \tag{3.4}$$

Here the assumption of non-degenerate eigenstates is essential in order to avoid the divergence in the denominator. By substituting this into Eq.

(3.3) and dividing the sum into two pieces, the equation of motion for the coefficient $c_m(t)$ reads

$$\dot{c}_m(t) = -\langle\psi_m(t)|\dot{\psi}_m(t)\rangle - \sum_n \frac{\langle\psi_m(t)|\dot{H}|\psi_n(t)\rangle}{E_n(t) - E_m(t)} \mathrm{e}^{-i(\theta_n(t)-\theta_m(t))}. \tag{3.5}$$

The first term of the equation is the adiabatic part, according to which the system remains in the same eigenstate it started from, whereas the latter term describes the diabatic excitations between the states. In case the latter term can be neglected, the evolution of the system is purely adiabatic resulting in the adiabatic equation of motion

$$\dot{c}_m(t) \approx -\langle\psi_m(t)|\dot{\psi}_m(t)\rangle. \tag{3.6}$$

The adiabatic approximation is justified if the diabatic contribution c_m^{d} to the evolution of the coefficients c_m in Eq. (3.5) is negligibly small,

$$\begin{aligned} c_m^{\mathrm{d}}(t) =& -\sum_n \frac{\langle\psi_m(t)|\dot{H}|\psi_n(t)\rangle}{E_n - E_m} \int_{-\infty}^{t} \mathrm{e}^{-i(\theta_n(t')-i\theta_m(t'))}\,\mathrm{d}t' \\ =& \hbar \sum_n \frac{\langle\psi_m(t)|\dot{H}|\psi_n(t)\rangle}{i\left(E_n - E_m\right)^2} \left[\mathrm{e}^{-i(\theta_n(t)-\theta_m(t))} - 1\right], \end{aligned} \tag{3.7}$$

where it has been assumed that $c_m^{\mathrm{d}}(-\infty)$ vanishes and that $|\psi_m(t)\rangle$, $\dot{H}$ and $E_n(t) - E_m(t)$ do not depend on time, which allows the integration over only the exponential part [42]. By applying Eq. (3.4) backwards, it can be seen that the diabatic contribution $|c_m^{\mathrm{d}}(t)|$ can be neglected if

$$\hbar \sum_n \left| \frac{\langle\psi_m(t)|\dot{\psi}_n(t)\rangle}{E_n - E_m} \right| \ll 1. \tag{3.8}$$

This inequality is known as the adiabatic condition, and can be widely applied in studying the feasibility of the adiabatic evolution [43]. Recently it has been shown that the above condition is not sufficient nor necessary condition for adiabatic evolution for a general system [44, 45], but for the results discussed in this thesis it is adequate.

Furthermore, the evolution of $\dot{c}_m(t)$ in the adiabatic approximation can be solved from Eq. (3.6) to yield

$$c_m(t) = c_m(-\infty)\mathrm{e}^{-\langle\psi_m(t)|\dot{\psi}_m(t)\rangle} = c_m(-\infty)\mathrm{e}^{i\gamma_m(t)}, \tag{3.9}$$

where $\gamma_m(t) = i\langle\psi_m(t)|\dot{\psi}_m(t)\rangle$ is called the geometric phase. The adiabatic wave function of the system can be calculated by substituting $c_m(t)$ to Eq. (3.1),

$$|\psi(t)\rangle = \sum_n c_n(-\infty)|\psi_n(t)\rangle \mathrm{e}^{-i\theta_n(t)+i\gamma_n(t)}. \tag{3.10}$$

The solution implies that the system stays in the same eigenstate it started from, but it acquires a phase factor $\zeta_n(t) = -\theta_n(t) + \gamma_n(t)$, where $\theta_n(t)$ is the dynamical phase which depends on the energies of the instantaneous eigenstates, and the geometric phase $\gamma_n(t)$ that only depends on the path the system has traversed. The geometric phase can be eliminated by a gauge transformation unless the path of the system makes a full loop, in which case the accumulated geometric phase becomes physically meaningful [46].

3.1 Stimulated Raman adiabatic passage in a three-level transmon

Building of a full-fledged quantum computer requires coupling of large number of quantum elements with each other [8]. Using multilevel systems instead of the standard two-level qubits enlarges the Hilbert space which can be employed for the computations, potentially allowing for a much more powerful computer to be build [47]. On the other hand, the larger Hilbert space supported by the multilevel systems can also be used to reduce the number of elements in the computer, simplifying its structure and therefore eliminating additional sources of decoherence.

The accurate state manipulation and preparation is a vital component of a quantum processor. One of the drawbacks of building a multilevel quantum processor is the increased difficulty to control its operation. There adiabatic methods can provide tools for robust state preparation, which is insensitive to the fluctuations in the control parameters. Stimulated Raman adiabatic passage (STIRAP) can be used to transfer the population over a forbidden transition [43, 48], which makes the protocol ideal for preparing the second excited state of a transmon.

Initially STIRAP was developed for controlling molecular and atomic systems, where it was important to be able to transfer population over a dissipative intermediate state. An interesting feature of STIRAP is that the intermediate state never gets populated, rendering the dissipative dynamics of the intermediate state irrelevant. In those systems STIRAP is usually used in a ladder configuration, where both the initial and the target state have lower energies than the intermediate state. In circuit QED such energy level structure does not appear naturally, and therefore it is the other features of STIRAP which make it appealing for solid-state systems: the state preparation accomplished by STIRAP is not sensitive to the amplitudes or the timings of the control pulses used to drive the

process. This eliminates the adverse effects of environmental fluctuations on the population transfer fidelity. In circuit QED, the fluctuations might result from noise of the electronics or unpredictable changes in the impedances of the control lines. The experimental conditions might also slowly change with time. Here robustness of the processes can help to mitigate the need to calibrate the system frequently.

STIRAP relies on two driving signals, which couple in 0–1 and 1–2 transitions of the qutrit. The driven Jaynes-Cummings Hamiltonian given in Eq. (2.14) can be taken as a starting point for the analysis. For now the off-resonant terms are neglected, and it is assumed that both drive frequencies are close to their corresponding transitions, yielding a driven Hamiltonian

$$\hat{H}'_{\mathrm{S}} = \hat{H}_{\mathrm{JC}} + \frac{\hbar}{2}\sum_{i=0,1}\Omega_{i,i+1}(t)|i\rangle\langle(i+1)|\mathrm{e}^{i(\omega^{\mathrm{d}}_{i,i+1}t+\phi_{i,i+1})} + \mathrm{h.c.} \tag{3.11}$$

In the STIRAP experiment the resonator is only used for the readout, and therefore its influence on the system dynamics can be ignored. In the three-level approximation the STIRAP Hamiltonian can be written

$$\hat{H}''_{\mathrm{S}} = \hbar\sum_{i=0,1,2}\omega_i|i\rangle\langle i| + \frac{\hbar}{2}\sum_{i=0,1}\Omega_{i,i+1}(t)|i\rangle\langle(i+1)|\mathrm{e}^{i(\omega^{\mathrm{d}}_{i,i+1}t+\phi_{i,i+1})} + \mathrm{h.c.}, \tag{3.12}$$

where $\omega_i \to \omega_i + \chi_{i-1}$ are the Lamb-shifted transmon transition frequencies from the dispersive Jaynes-Cummings Hamiltonian in Eq. (2.10). The Hamiltonian can be further simplified by moving into a doubly rotating frame, rotating with the two drives. The transformation is given by the unitary operator

$$\hat{U}_{\mathrm{rf}} = \hbar\omega_0|0\rangle\langle 0| + \hbar\sum_{i=1,2}\left(\sum_{j=0}^{i-1}\omega^{\mathrm{d}}_{j,j+1}\right)|i\rangle\langle i|, \tag{3.13}$$

which transforms the Hamiltonian as

$$\begin{aligned}\hat{H}_{\mathrm{S}} &= \hat{U}\hat{H}\hat{U}^{\dagger} + i\hbar\frac{\partial\hat{U}}{\partial t}\hat{U}^{\dagger} \\ &= \hbar\sum_{i=1,2}\sum_{j=0}^{i-1}\delta_{j,j+1}|i\rangle\langle i| + \frac{\hbar}{2}\sum_{i=0,1}\Omega_{i,i+1}(t)|i\rangle\langle(i+1)|\mathrm{e}^{i\phi_{i,i+1}} + \mathrm{h.c.} \\ &= \frac{\hbar}{2}\begin{bmatrix} 0 & \Omega_{01}(t)\mathrm{e}^{i\phi_{01}} & 0 \\ \Omega_{01}(t)\mathrm{e}^{-i\phi_{01}} & 2\delta_{01} & \Omega_{12}(t)\mathrm{e}^{i\phi_{12}} \\ 0 & \Omega_{12}(t)\mathrm{e}^{-i\phi_{12}} & 2(\delta_{01}+\delta_{12}) \end{bmatrix},\end{aligned} \tag{3.14}$$

where $\delta_{i,i+1} = \omega_{i+1} - \omega_i - \omega^{\mathrm{d}}_{i,i+1}$ are the detunings of the drives from their corresponding transitions and it is assumed that $\omega_0 = 0$. The ob-

jective of STIRAP is to make the system to adiabatically follow the initial state $|0\rangle$ which evolves to the target state $|2\rangle$. In order to find the instantaneous eigenstate that realizes the transformation as a function of the external parameters, the Hamiltonian in Eq. (3.14) can be diagonalized. Assuming that the drives satisfy the two-photon resonant condition $\delta_{01} + \delta_{12} = 0$, the diagonalization results in the eigenvalues $\omega_+ = \delta_{01} + \sqrt{\delta_{01}^2 + \Omega_{01}(t)^2 + \Omega_{12}(t)^2}$, $\omega_- = \delta_{01} - \sqrt{\delta_{01}^2 + \Omega_{01}(t)^2 + \Omega_{12}(t)^2}$, and $\omega_\mathrm{D} = 0$, with the corresponding eigenvectors

$$\begin{aligned} |+\rangle &= \sin\Phi|\mathrm{B}\rangle + \cos\Phi \mathrm{e}^{-\mathrm{i}\phi_{01}}|1\rangle, \\ |-\rangle &= \cos\Phi|\mathrm{B}\rangle - \sin\Phi \mathrm{e}^{-\mathrm{i}\phi_{01}}|1\rangle, \\ |\mathrm{D}\rangle &= \cos\Theta|0\rangle - \sin\Theta \mathrm{e}^{-i(\phi_{01}+\phi_{12})}|2\rangle, \end{aligned} \tag{3.15}$$

where the zero-eigenvalue state is called the dark state, and the state orthogonal to it $|\mathrm{B}\rangle = \sin\Theta|0\rangle + \cos\Theta \mathrm{e}^{-i(\phi_{01}+\phi_{12})}|2\rangle$ is referred to as the bright state. The angle Θ is defined by $\tan\Theta(t) = \Omega_{01}(t)/\Omega_{12}(t)$ and it parametrizes the rotation in the $\{|0\rangle, |2\rangle\}$ subspace, while

$$\Phi = \tan^{-1}\left[\frac{\sqrt{\Omega_{01}(t)^2 + \Omega_{12}(t)^2}}{\sqrt{\Omega_{01}(t)^2 + \Omega_{12}(t)^2 + \delta_{01}^2} + \delta_{01}}\right]. \tag{3.16}$$

In the case of resonant STIRAP ($\delta_{01} = \delta_{12} = 0$) the variable $\Phi = \pi/4$ is a constant. Initially the system is taken to be in the computational ground state $|0\rangle$. It is not obvious to what initial state in the instantaneous basis this corresponds to because $\Theta(t_\mathrm{i})$ is undefined if both $\Omega_{01}(t_\mathrm{i}) = \Omega_{12}(t_\mathrm{i}) = 0$, which is a realistic assumption. However, as soon as either of the amplitudes gets a non-zero value, $\Theta(t_\mathrm{i})$ can be defined, and it gives the initial state in the instantaneous basis. Therefore, if $\Omega_{12}(t)$ pulse is applied first, the mixing angle is $\Theta(t_\mathrm{i}) = 0$, which corresponds to the initial state $|\psi_\mathrm{i}\rangle = |D\rangle$. In the end of the STIRAP pulse sequence the amplitude $\Omega_{01}(t)$ approaches zero later than the $\Omega_{12}(t)$ amplitude, and the final mixing angle $\Theta_\mathrm{f} \to \frac{\pi}{2}$ and $|\psi_\mathrm{f}\rangle = |\mathrm{D}\rangle = |2\rangle$, realizing the required transformation. The choice of the initial state in the instantaneous basis signifies the importance of the pulse order in STIRAP: The pulses are applied in the counter-intuitive order, where the 1–2 transition is driven before 0–1 transition. If the intuitive order ($\Theta_\mathrm{i} = \frac{\pi}{2}$) were used, the initial state would be $|\psi_\mathrm{i}\rangle = \frac{1}{\sqrt{2}}(|+\rangle + |-\rangle)$ resulting in population in state $|1\rangle$ and an undesired final state.

The condition for the adiabatic following has been derived in Eq. (3.8),

which becomes [49]

$$\left| \frac{\dot{\Omega}_{01}(t)\Omega_{12}(t) - \Omega_{01}(t)\dot{\Omega}_{12}(t)}{[\Omega_{01}(t)^2 + \Omega_{12}(t)^2]^{3/2}} \right| \ll 1, \tag{3.17}$$

for the instantaneous eigenstates given in Eq. (3.15) with $\delta_{01} = \delta_{12} = 0$. If the condition is satisfied the system remains in state $|\mathrm{D}\rangle$ during the whole STIRAP protocol.

The requirements of the adiabatic excitation can be satisfied by many different pulse shapes. In principle the pulses only need to fulfill the initial and the final conditions for $\Theta(t)$ and the condition of adiabatic following in between. In the experiments presented in this thesis Gaussian pulse envelopes were used to manipulate the Hamiltonian,

$$\begin{aligned} \Omega_{01}(t) =& \Omega_{01} \exp\left[-\frac{t^2}{2\sigma^2}\right], \\ \Omega_{12}(t) =& \Omega_{12} \exp\left[-\frac{(t-t_s)^2}{2\sigma^2}\right], \end{aligned} \tag{3.18}$$

where t_s is the time separation between the maxima of the pulses, σ is the width of the pulses, and Ω_{01} and Ω_{12} are their peak amplitudes. In order to asses the adiabaticity of the STIRAP protocol with Gaussian pulse shapes, the global adiabatic condition can be found by integrating Eq. (3.17) over time

$$\frac{\pi}{2} \ll \int_{-\infty}^{\infty} \sqrt{\Omega_{01}(t)^2 + \Omega_{12}(t)^2}\, \mathrm{d}t. \tag{3.19}$$

The remaining integral does not have an analytic solution, but it can be shown that it is an increasing function of t_s; moreover, its values for the pulse separations $t_s = 0$ and $t_s = \infty$ and equal pulse amplitudes $\Omega_{01} = \Omega_{12} = \Omega$ can be calculated analytically, yielding $2\sqrt{\pi}\sigma\Omega$ and $2\sqrt{2\pi}\sigma\Omega$, respectively. Thus, by selecting the minimum value $2\sqrt{\pi}\sigma\Omega$ one obtains the constraint

$$\frac{4}{\sqrt{\pi}}\sigma\Omega \gg 1. \tag{3.20}$$

The global adiabatic condition only gives a simplified picture of the adiabaticity, because it does not take into account the severity of the consequences of violating the condition on population transfer. For example, the violations of the adiabatic condition at times where the pulse amplitudes are small are less harmful, because the evolution of the system is slow. However, the global adiabatic condition is useful for qualitative analysis on the relation between the pulse parameters and the adiabaticity of the process. The global adiabatic condition shows that the transfer efficiency can be improved by making the duration of the pulses longer

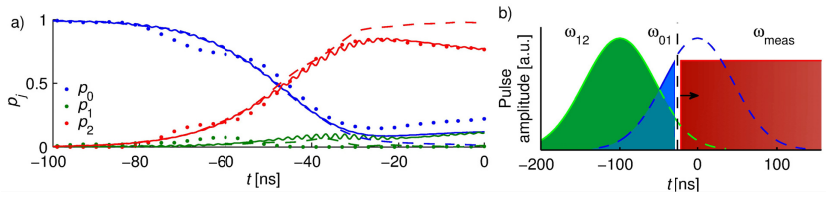

Figure 3.1. a) The state of the transmon at different times during STIRAP. The dots represent experimental results, the dashed line is a simulation of the three-level dissipationless case, and the continuous lines shows the simulation with the dissipation included. During the time evolution the intermediate state $|1\rangle$ remains almost unpopulated. b) Schematic of the pulse sequence used in STIRAP. The time evolution is measured by interrupting the STIRAP pulses at different times. Figure from Publication VI.

or by increasing their amplitude. The pulse overlap parameter t_s/σ also plays a role in the adiabaticity of the process, but that is not captured by the global condition.

If high transfer fidelity is of priority, it is possible to find more effective pulse shapes than Gaussian pulses. For example, the pulse shape can be optimized based on the local adiabatic condition, resulting in slightly faster population transfer [50]. The transfer fidelity can also be improved using composite pulses, where several STIRAP sequences with switching pulse order are applied in series [51].

In Publication VI we have realized a STIRAP experiment in a three-level transmon with the ladder energy level configuration. Fig. 3.1a) shows the occupation probabilities of the qutrit state $|\psi(t)\rangle = \alpha(t)|0\rangle + \beta(t)|1\rangle + \gamma(t)|2\rangle$ during STIRAP, where the probabilities are defined using the Born rule $p_0(t) = |\alpha(t)|^2$, $p_1(t) = |\beta(t)|^2$, and $p_2(t) = |\gamma(t)|^2$. The measured experimental points are shown as dots, whereas the solid line describes a matching numerical simulation performed using the Hamiltonian in Eq. (3.11) (see Sec. 6.1 for additional information). The dashed line corresponds to a simulation where decoherence is ignored. The experiment reveals the most distinct characteristic of STIRAP: There is almost no population in state $|1\rangle$ during the population transfer, which confirms that the system follows the dark state $|\mathrm{D}\rangle$. The population of the state $|2\rangle$ reaches 83 %, where most of the infidelity can be attributed to the decoherence, which is proven by the simulations with and without decoherence.

3.1.1 Robustness to control parameters

In the circuit QED realization of STIRAP its most important feature is the robustness to the fluctuations and mistakes in the control parame-

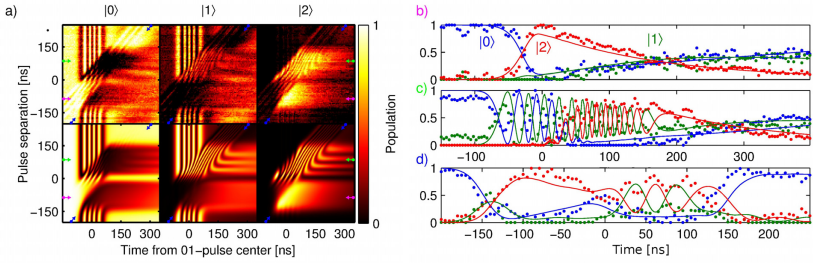

Figure 3.2. a) Evolution of the occupation probabilities $p_0(t)$, $p_1(t)$, and $p_2(t)$ during the STIRAP experiment as a function of the pulse separation t_s. The upper panels show the experimental result supported by the numerical simulation shown in the lower panels. b) Evolution of the occupation probabilities along the trace marked by purple arrows in a). The relative pulse separation $t_\mathrm{s}/\sigma = -2$ is negative, corresponding to the counter-intuitive pulse sequence. c) Time trace along the path marked by the green arrows in a). The positive pulse separation $t_\mathrm{s}/\sigma = 2$ leads to oscillating behaviour. d) Time trace along the path marked by the blue arrows in a). The trace shows that the STIRAP transfer fidelity is a slowly varying function for negative values of t_s/σ, which means that the process is robust with respect to small mistakes in t_s. The pulse width used in the experiment is $\sigma = 50$ ns. The dots are experimental results whereas the solid lines correspond to a numerical simulation. Figure adapted from Publication VI.

ters such as the pulse amplitudes Ω_{01} and Ω_{12} or the separation time between the pulses t_s. The insensitivity to the control parameters results from the adiabatic nature of the population transfer: only the initial and the final conditions of the eigenstates are important, and they can usually be asymptotically satisfied. The robustness of STIRAP with respect to the pulse overlap is demonstrated in the experiment shown in Fig. 3.2a), where the pulse separation between the pulses is varied and the evolution of the states' populations is recorded. For the counter-intuitive pulse sequence ($t_\mathrm{s} < 0$) a high population transfer fidelity is reached for a wide range of values for pulse separation (Fig. 3.2d)). At $t_\mathrm{s} = 0$ a rapid change in the behaviour occurs. Due to the complete overlap of the pulses $\Theta(t_\mathrm{i}) \neq 0$, which leads to the change of the initial eigenstate in the adiabatic basis. This causes the oscillating behaviour for the positive values of t_s.

Interestingly, STIRAP is also robust to the detunings of the driving fields from their corresponding transitions. The robustness is most pronounced if the two-photon resonance condition $\delta_{01} = -\delta_{12}$ is fulfilled [52], *i.e.* the sum of the drive frequencies matches the ω_{02} transition frequency. Experimentally this is shown in Fig. 3.3a), where the diamond like feature corresponds to the region of high population transfer and there is a clear broadening along the axis where the two-photon resonance condition

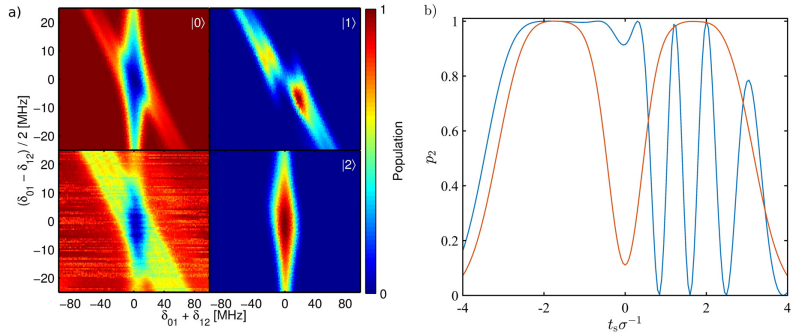

Figure 3.3. a) State $|0\rangle$ occupation probability in a STIRAP experiment as a function of the single-photon (vertical axis) and two-photon (horizontal axis) detunings is shown in the lower left panel. The other panels show the corresponding simulation results for p_0, p_1 and p_2. Figure from Publication VI. b) Simulation of the state $|2\rangle$ occupation probability p_2 as a function of the relative pulse overlap t_s/σ in case of resonant STIRAP (blue) or with single-photon detuning $\delta = 0.6\,\Omega$ (red).

is satisfied.

3.1.2 Bright STIRAP

Applying STIRAP with single photon detuning can be used to remove the condition of the counter-intuitive pulse order. For the intuitive pulse order ($t_\mathrm{s} > 0$) the population transfer by standard STIRAP fails because the initial state in the adiabatic basis is given by $|\psi_\mathrm{i}\rangle = \frac{1}{\sqrt{2}}(|-\rangle + |+\rangle)$. However, by taking the detuning $\delta \gg \Omega(t_\mathrm{i})$, the angle $\Phi(t_\mathrm{i}) \approx 0$ and the initial state becomes $|\psi_\mathrm{i}\rangle = |-\rangle = |\mathrm{B}\rangle$. The method is called bright STIRAP (b-STIRAP) [53], because in contrast to the standard STIRAP, here the population transfer is realized by following the bright state $|\mathrm{B}\rangle$. If the condition $\delta \gg \Omega(t_\mathrm{f})$ is also satisfied at the end of the sequence, the resulting final state is $|\psi_\mathrm{f}\rangle = |2\rangle$, because for the intuitive pulse order $\Theta(t_\mathrm{i}) = \pi/2$ evolves to $\Theta(t_\mathrm{f}) = 0$. The action of single photon detuning is demonstrated in Fig. 3.3b), where the blue line shows the population of state $|2\rangle$ after a resonant STIRAP as a function of the pulse separation (negative values correspond to counter-intuitive pulse order), replicating the experimental result of Fig. 3.2d). The red line shows the off-resonant case, where two plateaus form instead, located at positive and negative values of $t_\mathrm{s} \approx \pm 1.5\sigma$. However, the width of the plateau is slightly smaller than the width of the plateau in the resonant case, because the effective pulse overlap area is reduced due to the detuning [54]. Interestingly, b-STIRAP can also be applied to perform population inversion for an arbitrary initial

state in the $\{|0\rangle, |2\rangle\}$ subspace. The system initially in the superposition state $|\psi_\mathrm{i}\rangle = \alpha|0\rangle + \gamma|2\rangle$ has the initial state in the instantaneous basis given by $|\psi_\mathrm{i}\rangle = \alpha|\mathrm{D}\rangle + \gamma|\mathrm{B}\rangle$ if counter-intuitive pulse order is assumed. During the process, the state evolves to $|\psi_\mathrm{f}\rangle = \alpha|\mathrm{D}\rangle + \beta|\mathrm{B}\rangle \mathrm{e}^{\mathrm{i}\phi_\mathrm{f}} = \gamma|0\rangle - \alpha|2\rangle \mathrm{e}^{\mathrm{i}\phi_\mathrm{f}}$, where ϕ_f is the accumulated dynamical phase resulting from $|\mathrm{B}\rangle$ not being a zero energy state. In Sec. 4.4 this property is applied in realizing a robust NOT-gate.

3.1.3 Fractional STIRAP

Fractional STIRAP (f-STIRAP) can be used to create superpositions between the states $|0\rangle$ and $|2\rangle$. The method was initially discovered in [55] and further developed in [56]. The simplest way to realize the fractional STIRAP is to interrupt the pulse sequence at a given moment, which leads to freezing of the evolution [57]. This method is very sensitive to the moment of interruption, which is why more elegant methods have been developed. In smooth f-STIRAP the pulse shapes are modified so that in the end of the sequence the mixing angle $\Theta(\infty)$ has the desired value. This is accomplished by limiting the amplitude of the 0–1 pulse and adding a second pulse on the 1–2 transition,

$$\begin{aligned} \Omega_{01}^\mathrm{F}(t) &= \sin(\eta)\Omega_{01}(t), \\ \Omega_{12}^\mathrm{F}(t) &= \Omega_{12}(t) + \cos(\eta)\Omega_{01}(t), \end{aligned} \tag{3.21}$$

which gives $\Theta(\infty) = \eta$. The final state $|\psi_\mathrm{f}\rangle = \cos\eta|0\rangle - \mathrm{e}^{-i(\phi_{01}+\phi_{12})}\sin\eta|2\rangle$ can be obtained by substituting $\Theta(\infty)$ into the definition of the dark state $|\mathrm{D}\rangle$ in (3.15). Optionally, when applied simultaneously with b-STIRAP also the initial mixing angle can be modified by adding the second pulse to the 0–1 transition instead.

3.1.4 Cross coupling of the drives

In transmon, the drive signals used to control the quantum state do not only couple to the target transitions, but off-resonantly drive every other transition in the system. Usually the off-resonant driving can be neglected due to the drive amplitude being small with respect to the detuning. However, in transmon the anharmonicity is relatively small, which makes the couplings significant. The issue is not specific to adiabatic control, and it is present also with direct Rabi pulses. There exists clever solutions which try to mitigate the effect in the control of two-level systems, such as derivative removal by adiabatic gate [58].

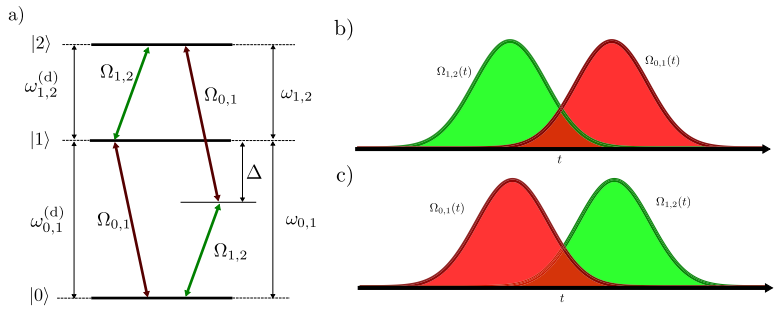

Figure 3.4. a) Energy level diagram of a qutrit driven by two drives with frequencies $\omega_{01}^{(d)}$ and $\omega_{12}^{(d)}$ and peak amplitudes Ω_{01} and Ω_{12}. Due to the cross-coupling of the drives, an additional STIRAP with the single photon detuning $\delta = \Delta$ forms. Figure from Publication IV. b) Pulse shapes of the actual STIRAP process. c) Pulse shapes of the parasitic STIRAP.

In STIRAP the problem turns out to be particularly problematic because of its inherent robustness to the single photon detuning [52]. The off-resonant couplings form another STIRAP process, which also satisfies the two-photon resonance condition, demonstrated in Fig. 3.4a). The pulse order of the parasitic STIRAP is reversed (Fig. 3.4b) and c)), but it still can support population transfer through b-STIRAP, which is robust to single photon detuning. These two STIRAP processes compete against each other so that if the parasitic process becomes relevant, the population of state $|2\rangle$ after the process is reduced. Effectively this limits the drive amplitudes Ω_{01} and Ω_{12}, and therefore the duration of the STIRAP pulses must be increased in order to satisfy the adiabatic condition. In Publication IV we show that in the presence of energy relaxation the trade-off gives rise to an optimal choice for STIRAP pulse amplitudes. This is demonstrated in Fig. 3.5, where the amplitudes $\Omega = \Omega_{01} = \Omega_{12}$ and the pulse widths σ are varied so that the inverse adiabaticity $a = \Omega\sigma = 3\pi$ is constant. In case the cross-couplings or decoherence are not included in the simulation, only a determines the success rate of the STIRAP, resulting in a constant population in state $|2\rangle$ (blue line). If the cross-couplings are included the success rate drops for higher values of Ω (red line), resulting in a conclusion that it is beneficial to use long and low intensity pulses for STIRAP. However, when also decoherence is included (dashed lines), an optimal ratio of Ω and σ can be found. The cross-couplings start to significantly affect p_2 when $\Omega \approx \Delta/2$.

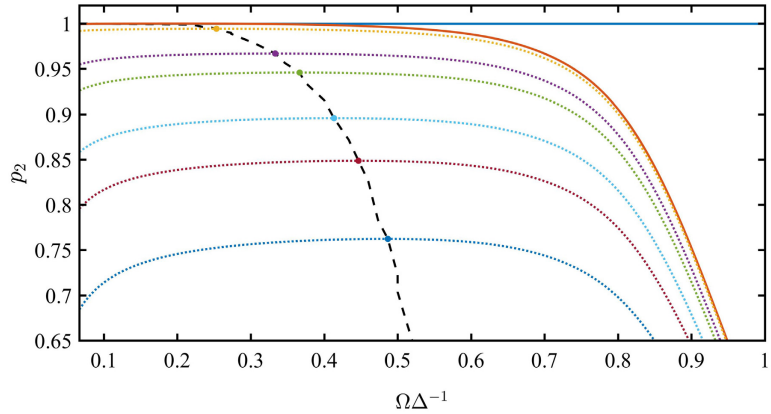

Figure 3.5. A numerical simulation of the population p_2 after STIRAP in absence of the cross couplings (blue line) and in the presence of cross couplings (red line). The amplitudes Ω are normalized with the anharmonicity Δ. The dashed lines show p_2 in the presence of decoherence corresponding to values $2\pi\Gamma\Delta^{-1} * 10^{-4} = \{1, 10, 20, 30, 50, 100\}$. The dashed black line marks the optimum value of Ω for different decoherence rates. Figure from Publication IV.

3.1.5 Hybrid Rabi-STIRAP pulses

Preceding the STIRAP pulses with a Rabi pulse acting on 0–1 transition can be used to study the evolution of the system initially in an arbitrary superposition of $|0\rangle$ and $|1\rangle$ states, $|\psi_\mathrm{i}\rangle = \alpha|0\rangle + \beta|1\rangle$. In Publication VI we have experimentally realized such pulse sequence, and in Publication V we have shown that the hybrid pulses can be used to create arbitrary superpositions of the qutrit states. In the instantaneous eigenbasis the initial state is given by $|\psi_\mathrm{i}\rangle = \alpha|\mathrm{D}\rangle + \frac{\beta}{\sqrt{2}}\mathrm{e}^{\mathrm{i}\phi_{01}}(|+\rangle - |-\rangle)$, where there is contribution from both the states $|+\rangle$ and $|-\rangle$. According to Eq. (3.10) the time evolution during the STIRAP part is given by $|\psi(t)\rangle = \alpha|\mathrm{D}\rangle + \frac{\beta}{\sqrt{2}}\mathrm{e}^{\mathrm{i}\phi_{01}}\left(|+\rangle\mathrm{e}^{\mathrm{i}\zeta_+(\mathrm{t})} - |-\rangle\mathrm{e}^{\mathrm{i}\zeta_-(\mathrm{t})}\right)$, where adiabatic evolution is assumed and the phases acquired by the eigenstates are given by the dynamical part $\zeta_j = -\int_{-\infty}^{t}\omega_j\,\mathrm{d}t$, where $j = \{\mathrm{D}, +, -\}$. For STIRAP eigenstates the geometric phase from Eq. (3.10), $\gamma_j = i\langle j|\frac{\mathrm{d}j}{\mathrm{d}t}\rangle = 0$ vanishes. Because the states $|+\rangle$ and $|-\rangle$ are not zero-energy states, they accumulate phases during the evolution leading to interference characterized by $\Omega_\mathrm{S} = \int_{-\infty}^{\infty}\sqrt{\Omega_{01}(t)^2 + \Omega_{12}(t)^2} = \pm\zeta_\mp$ for resonant STIRAP. After the STIRAP pulses, the state in the computational basis is

$$|\psi_\mathrm{f}\rangle = -\beta\mathrm{e}^{i\phi_{01}}\sin\left(\frac{1}{2}\Omega_\mathrm{S}\right)|0\rangle + \beta\cos\left(\frac{1}{2}\Omega_\mathrm{S}\right)|1\rangle - \alpha\mathrm{e}^{-i(\phi_{01}+\phi_{12})}|2\rangle. \quad (3.22)$$

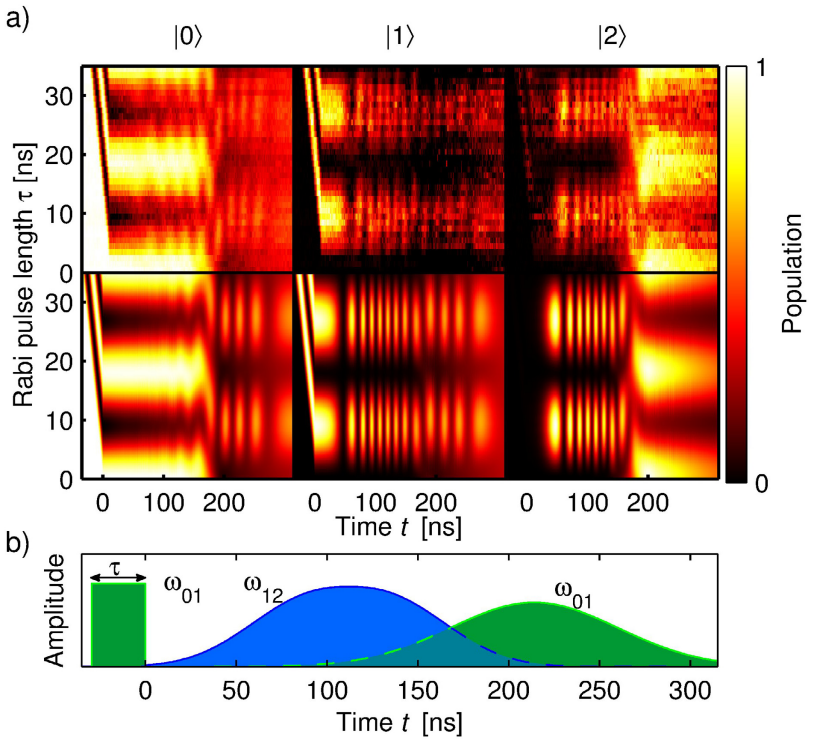

Figure 3.6. a) Occupation probabilities of the states $|0\rangle$, $|1\rangle$, and $|2\rangle$ during the hybrid Rabi-STIRAP pulse sequence. The upper panels show the experimental result, supported by the simulation shown in the lower panels. The coefficients α and β are controlled by the length of the Rabi pulse τ. b) The pulse sequence used to realize the experiment. First a π-pulse is applied on 0–1 transition, which is followed by the STIRAP pulses. Figure from Publication VI.

Fig. 3.6a) shows the experiment and the corresponding simulation where the combined pulse sequence (Fig. 3.6b)) is applied to the transmon. The length of the Rabi pulse, τ, determines the initial coefficients α and β, which are further subjected to STIRAP. The experimental results are well captured by the simulation, which confirms that the adiabatic process can be accurately controlled in the experiment. Thus we have demonstrated that the population initially in the ground state is fully transferred to state $|2\rangle$, and the remaining population is divided between the states $|0\rangle$ and $|1\rangle$ as given by Eq. (3.22). According to Eq. (3.22), the phase of the resulting qutrit state can also be fully controlled with the phases of the STIRAP pulses ϕ_{01} and ϕ_{12}. The result is useful in cases where 0–1 transition can be accurately controlled, but robustness is required in 0–2 transition due to the experimental conditions.

4. Superadiabatic population transfer

The adiabatic control of the quantum state is a powerful concept, which enables robust state preparation. The main drawback of the approach is the long duration of the pulses because of the requirement of adiabaticity. During the recent years there have been several suggestions on speeding up the adiabatic protocols. In Refs. [59] and [60] it was shown that it is possible to modify the Hamiltonian so that the system follows the exact adiabatic path even though the condition for adiabatic evolution is not satisfied. By adding a counter-diabatic term to the Hamiltonian [61, 62], the transitions between the instantaneous eigenstates can be completely suppressed, which is why the method is called transitionless [60] or superadiabatic [63] driving. In Publication III we have experimentally realized the superadiabatic protocol in a three-level transmon using STIRAP.

The superadiabatic driving is based on designing the counter-diabatic Hamiltonian $\hat{H}_{\mathrm{cd}}$, which is derived by reverse engineering the adiabatic evolution of the original Hamiltonian $\hat{H}_0$. Assuming that the adiabatic approximation is valid, the time evolution of the system under the Hamiltonian $\hat{H}_0$ is given by Eq. (3.10). The equation can be interpreted as a solution to the Schrödinger equation

$$|\psi(t)\rangle = \hat{U}(t,t')|\psi(t')\rangle, \tag{4.1}$$

with $\hat{U}(t,t')$ defined as

$$\hat{U}(t,t') = \sum_n |\psi_n(t)\rangle\langle\psi_n(t')|\mathrm{e}^{i\zeta_n(t)}, \tag{4.2}$$

where $\zeta_n(t)$ is the acquired phase and $|\psi_n(t)\rangle$ are the instantaneous eigenstates of $\hat{H}_0$. The Hamiltonian $\hat{H}$ that generates the desired time evolution can be reverse engineered by multiplying both sides of Eq. (4.1) by

$\hat{H}$, yielding

$$\begin{aligned}
\hat{H}|\psi(t)\rangle = \hat{H}\hat{U}(t,t')|\psi(t')\rangle \implies \\
i\hbar|\dot{\psi}(t)\rangle = \hat{H}\hat{U}(t,t')|\psi(t')\rangle \implies \\
i\hbar\dot{\hat{U}}(t,t')|\psi(t')\rangle = \hat{H}\hat{U}(t,t')|\psi(t')\rangle \implies \\
i\hbar\dot{\hat{U}}(t,t') = \hat{H}\hat{U}(t,t') \implies \\
\hat{H} = i\hbar\dot{\hat{U}}(t,t')\hat{U}^{\dagger}(t,t'). \qquad (4.3)
\end{aligned}$$

After substitution of $\hat{U}(t,t')$ given in Eq. (4.2), the Hamiltonian becomes

$$\begin{aligned}
\hat{H} =& i\hbar\sum_n \Big(|\dot{\psi_n}(t)\rangle\langle\psi_n(t)| + i\dot{\zeta_n}|\psi_n(t)\rangle\langle\psi_n(t)|\Big) \\
=& i\hbar\sum_n \Big(|\dot{\psi_n}(t)\rangle\langle\psi_n(t)| - \langle\psi_n(t)|\dot{\psi_n}(t)\rangle|\psi_n(t)\rangle\langle\psi_n(t)|\Big) \\
&+ \sum_n E_n(t)|\psi_n(t)\rangle\langle\psi_n(t)|, \qquad (4.4)
\end{aligned}$$

where the last sum gives $\hat{H}_0$, and the first sum can be identified as the additional counterdiabatic Hamiltonian $\hat{H}_{\mathrm{cd}}$, which guarantees that the evolution of the state under the new Hamiltonian follows the same path as the evolution of the state under the Hamiltonian $\hat{H}_0$ in the adiabatic approximation. Consequently, the evolution under $\hat{H}$ is not restricted by the adiabatic condition, which allows for fast high fidelity population transfer. This is especially advantageous in circuit QED, where decoherence is one of the main limiting factors to applying adiabatic methods.

4.1 Superadiabatic STIRAP

The superadiabatic method can be used to speed up the population transfer of STIRAP [64]. Most importantly, the superadiabatic method ideally provides unit fidelity in finite time as opposed to standard adiabatic methods, where high fidelity is only reached asymptotically. This is significant in advanced quantum information processing applications, such as quantum error correction [65], where extremely high fidelities are required. In addition, circuit QED provides a perfect test platform for superadiabatic methods, because using microwave technology the creation of highly coherent complicated control sequences is feasible.

The control pulses required to realize the counterdiabatic Hamiltonian $\hat{H}_{\mathrm{cd}}$ in the case of STIRAP can be evaluated by substituting the STIRAP eigenstates given in Eq. (3.15) to Eq. (4.4). In order to simplify the calculation, the phases ϕ_{01} and ϕ_{12} can be eliminated from the eigenstates by

transforming the STIRAP Hamiltonian $\hat{H}_{\mathrm{S}}$ with a unitary transformation

$$\hat{U}_{\phi} = \begin{bmatrix} 1 & 0 & 0 \\ 0 & \mathrm{e}^{i\phi_{01}} & 0 \\ 0 & 0 & \mathrm{e}^{i(\phi_{12}+\phi_{01})} \end{bmatrix}, \tag{4.5}$$

resulting in

$$\hat{H}''_{\mathrm{S}} = \hat{U}_{\phi}\hat{H}'_{\mathrm{S}}\hat{U}^{\dagger}_{\phi} = \frac{\hbar}{2}\begin{bmatrix} 0 & \Omega_{01}(t) & 0 \\ \Omega_{01}(t) & 2\delta_{01} & \Omega_{12}(t) \\ 0 & \Omega_{12}(t) & 2(\delta_{01}+\delta_{12}) \end{bmatrix}. \tag{4.6}$$

In this frame, the counterdiabatic part yields [66]

$$\hat{H}_{\mathrm{cd}} = i\hbar \begin{bmatrix} 0 & \sin(\Theta(t))\dot{\Phi}(t) & \dot{\Theta}(t) \\ -\sin(\Theta(t))\dot{\Phi}(t) & 0 & -\cos(\Theta(t))\dot{\Phi}(t) \\ -\dot{\Theta}(t) & \cos(\Theta(t))\dot{\Phi}(t) & 0 \end{bmatrix}, \tag{4.7}$$

which simplifies to

$$\hat{H}_{\mathrm{cd}} = i\hbar \begin{bmatrix} 0 & 0 & \dot{\Theta}(t) \\ 0 & 0 & 0 \\ -\dot{\Theta}(t) & 0 & 0 \end{bmatrix}, \tag{4.8}$$

if resonant STIRAP $\delta_{01} = \delta_{12} = 0$ is assumed. This implies that in order to realize the counterdiabatic driving an additional pulse coupling in the 0–2 transition is required. In standard STIRAP, the mixing angle is independent of the phases ϕ_{01} and ϕ_{12} and therefore they do not affect the population transfer as long as they are constant during the process [67]. On the contrary, in the superadiabatic method the population transfer is based on the (possibly) non-adiabatic evolution under the Hamiltonian $\hat{H}'_{\mathrm{SA}} = \hat{H}''_{\mathrm{S}} + \hat{H}_{\mathrm{cd}}$, with a strict phase dependence between the drives. The phase dependence in the original frame can be solved by transforming the Hamiltonian $\hat{H}'_{\mathrm{SA}}$ with the reverse unitary $U^{\dagger}_{\phi}$

$$\hat{H}_{\mathrm{SA}} = \hat{U}^{\dagger}_{\phi}\hat{H}'_{\mathrm{SA}}\hat{U}_{\phi} = \frac{\hbar}{2}\begin{bmatrix} 0 & \Omega_{01}(t)\mathrm{e}^{i\phi_{01}} & \Omega_{02}(t)\mathrm{e}^{i\phi_{02}} \\ \Omega_{01}(t)\mathrm{e}^{-i\phi_{01}} & 2\delta_{01} & \Omega_{12}(t)\mathrm{e}^{i\phi_{12}} \\ \Omega_{02}(t)\mathrm{e}^{-i\phi_{02}} & \Omega_{12}(t)\mathrm{e}^{-i\phi_{12}} & 2(\delta_{01}+\delta_{12}) \end{bmatrix}, \tag{4.9}$$

where $\Omega_{02}(t) = 2\dot{\Theta}(t)$ and $\phi_{02} = \phi_{01} + \phi_{12} + \pi/2$.

The appearance of the 0–2 coupling can be considered a drawback of the method, which has this far prevented its implementation in three-level systems, because the 0–2 transition might be forbidden and accurate phase coherence between the drives is needed. Alternatives for avoiding

the issue of the additional coupling has been developed based on Lewis-Riesenfeld invariants [68], where instead of following the adiabatic path, the system is guaranteed to meet the conditions for the initial and the final states. The benefit of that method is that no additional control pulses are needed, but it is enough to modify the pulse shapes of the existing pulses acting on 0–1 and 1–2 transitions. Another possibility is to modify the pulse shapes in a way which approximately leads to adiabatic following, which is experimentally verified in [69] for cold atoms, or to perform the accelerated population transfer in a dressed state basis [70, 71].

In Publication III we have managed to avoid the obstacle caused by the forbidden transition by employing a two-photon process to realize an effective 0–2 coupling. That allowed us to implement the superadiabatic STIRAP protocol (saSTIRAP) in a three-level system. In many cases multiphoton processes are unsuitable for fast control of quantum systems because the effective two-photon coupling is relatively small. However, in saSTIRAP the area of the counterdiabatic correction pulse is usually significantly smaller than the area of the STIRAP pulses, which compensates for the weaker coupling. This can be seen by integrating the counterdiabatic pulse area $\int_{-\infty}^{\infty} \Omega_{02}(t)\mathrm{d}t = 2(\Theta(\infty) - \Theta(-\infty)) = \pi$, which is much smaller than the STIRAP pulse areas usually employed ($\approx 5\pi$). However, there are several details that need to be taken into account when using two-photon driving, which are discussed in the next section.

4.1.1 Two-photon driving

The two-photon coupling is realized by introducing an additional drive with frequency $\omega_{2\mathrm{ph}}^{\mathrm{d}} \approx \omega_{02}/2$ so that the frequencies of the two photons of the drive add up to match the frequency of the target transition. The Hamiltonian describing the three-level system under two-photon driving in the frame rotating with the drive frequency $\omega_{2\mathrm{ph}}^{\mathrm{d}}$ can be written as

$$\hat{H}_{2\mathrm{ph}} = \hbar/2 \begin{bmatrix} 0 & \Omega_{2\mathrm{ph}}(t) & 0 \\ \Omega_{2\mathrm{ph}}^{*}(t) & 2\delta_{2\mathrm{ph}} & \lambda\Omega_{2\mathrm{ph}}(t) \\ 0 & \lambda\Omega_{2\mathrm{ph}}^{*}(t) & 4\delta_{2\mathrm{ph}} - 2\Delta \end{bmatrix}, \tag{4.10}$$

where λ is the factor describing the different coupling strengths of the drive on 0–1 and 1–2 transitions and the detuning $\delta_{2\mathrm{ph}} = \omega_{01} - \omega_{2\mathrm{ph}}^{\mathrm{d}}$. In case $\delta_{2\mathrm{ph}} \gg \Omega_{2\mathrm{ph}}(t)$ the two-photon drive can be considered far-detuned from both the 0–1 and 1–2 transitions and it is possible to apply adiabatic elimination [72] to derive an effective Hamiltonian in the $\{|0\rangle, |2\rangle\}$

subspace. The Schrödinger equation for the Hamiltonian (4.10) is

$$\begin{aligned} i\dot{\alpha} =& \frac{\beta\Omega_{2\mathrm{ph}}(t)}{2}, \\ i\dot{\beta} =& \frac{\alpha\Omega^*_{2\mathrm{ph}}(t)}{2} + \beta\delta_{2\mathrm{ph}} + \frac{\gamma\lambda\Omega_{2\mathrm{ph}}(t)}{2}, \\ i\dot{\gamma} =& \frac{\beta\lambda\Omega^*_{2\mathrm{ph}}(t)}{2} + \gamma(2\delta_{2\mathrm{ph}} - \Delta), \end{aligned} \tag{4.11}$$

where it can be assumed that the state $|1\rangle$ population is constant due to off-resonant driving, $\dot{\beta} = 0$. With that assumption the coefficient β can be solved to yield

$$\beta = -\frac{\alpha\Omega^*_{2\mathrm{ph}}(t) + \gamma\lambda\Omega_{2\mathrm{ph}}(t)}{2\delta_{2\mathrm{ph}}} \tag{4.12}$$

and by substituting this back to Eq. (4.11), the effective two-dimensional Hamiltonian can be written

$$\hat{H}_{2\mathrm{d}} = \frac{\hbar}{2}\begin{bmatrix} -\frac{|\Omega_{2\mathrm{ph}}(t)|^2}{2\delta_{2\mathrm{ph}}} & -\frac{\lambda\Omega^2_{2\mathrm{ph}}(t)}{2\delta_{2\mathrm{ph}}} \\ -\frac{\lambda\Omega^{*2}_{2\mathrm{ph}}(t)}{2\delta_{2\mathrm{ph}}} & 4\delta_{2\mathrm{ph}} - 2\Delta - \frac{\lambda^2|\Omega_{2\mathrm{ph}}(t)|^2}{2\delta_{2\mathrm{ph}}} \end{bmatrix}. \tag{4.13}$$

From the Hamiltonian one finds the effective two-photon coupling

$$\Omega_{\mathrm{eff}} = -\frac{\lambda\Omega^2_{2\mathrm{ph}}(t)}{2\delta_{2\mathrm{ph}}}. \tag{4.14}$$

In order to approximately understand how weak the coupling is with respect to a direct 0–2 coupling, Ω_{eff} can be evaluated with experimentally feasible values $\Omega_{2\mathrm{ph}}/(2\pi) = 50$ MHz, $\delta_{2\mathrm{ph}} = \Delta/2 = 150$ MHz and $\lambda = \sqrt{2}$, which yields $\Omega_{\mathrm{eff}}/(2\pi) \approx 12$ MHz and thus $\Omega_{\mathrm{eff}}/\Omega_{2\mathrm{ph}} \approx 24\%$. This is in the same scale as the usual ratio between the STIRAP pulse area and the counterdiabatic pulse area.

In the effective Hamiltonian there are additional terms on the diagonal. They are the ac-Stark shifts resulting from the mixing of the eigenstates $|0\rangle$, $|1\rangle$ and $|2\rangle$ caused by the off-resonant driving. Even though the shifts are quite small, they are significant in saSTIRAP because all the drives are required to maintain phase coherence with respect to each other. The time varying shifts result in accumulated phases, which break the phase coherence if not taken into account properly. The effective Hamiltonian approximately gives the shifts in the energies of $|0\rangle$ and $|2\rangle$ states, but perturbation theory can be used to calculate the shifts for all the states. Time-independent perturbation theory can be used if the coupling parameters $\Omega_{2\mathrm{ph}}(t)$ can be taken as slow functions in time, which is the case in the context of adiabatic methods. The two-photon driving Hamiltonian in Eq. (4.10) can be written $\hat{H}_{2\mathrm{ph}} = \hat{H}_0 + \hat{V}$, where $\hat{H}_0$ contains the diagonal elements of the Hamiltonian and $\hat{V}$ is the perturbation Hamiltonian

constructed from the off-diagonal elements. According to the second order perturbation theory, the corrected energies of the states are given by

$$\tilde{E}_n = E_n + \langle n|\hat{V}|n\rangle + \sum_{k\neq n} \frac{\langle k|\hat{V}|n\rangle}{E_n - E_k}, \tag{4.15}$$

where E_n are the eigenenergies of the unperturbed Hamiltonian $\hat{H}_0$. The shifts in the energies $\hbar\epsilon_n = \tilde{E}_n - E_n$ due to the correction are

$$\begin{aligned}
\epsilon_0(t) &= -\frac{|\Omega_{2\mathrm{ph}}(t)|^2}{4\delta_{2\mathrm{ph}}}, \\
\epsilon_1(t) &= \frac{|\Omega_{2\mathrm{ph}}(t)|^2}{4\delta_{2\mathrm{ph}}} + \frac{\lambda^2|\Omega_{2\mathrm{ph}}(t)|^2}{4(\Delta-\delta_{2\mathrm{ph}})}, \\
\epsilon_2(t) &= -\frac{\lambda^2|\Omega_{2\mathrm{ph}}(t)|^2}{4(\Delta-\delta_{2\mathrm{ph}})},
\end{aligned} \tag{4.16}$$

which further induce shifts in the transition frequencies $\hbar\epsilon_{n,n+1}(t) = \epsilon_{n,n+1} - \epsilon_n$,

$$\begin{aligned}
\epsilon_{01}(t) &= \frac{|\Omega_{2\mathrm{ph}}(t)|^2}{2\delta_{2\mathrm{ph}}} + \frac{\lambda^2|\Omega_{2\mathrm{ph}}(t)|^2}{4(\Delta-\delta_{2\mathrm{ph}})}, \\
\epsilon_{12}(t) &= -\frac{|\Omega_{2\mathrm{ph}}(t)|^2}{4\delta_{2\mathrm{ph}}} - \frac{\lambda^2|\Omega_{2\mathrm{ph}}(t)|^2}{2(\Delta-\delta_{2\mathrm{ph}})}, \\
\epsilon_{02}(t) &= \frac{|\Omega_{2\mathrm{ph}}(t)|^2}{4\delta_{2\mathrm{ph}}} - \frac{\lambda^2|\Omega_{2\mathrm{ph}}(t)|^2}{4(\Delta-\delta_{2\mathrm{ph}})}.
\end{aligned} \tag{4.17}$$

Furthermore, the accumulated extra phases due to the ac-Stark shifts are determined by the integrals

$$\tilde{\phi}_{i,i+1}(t) = \int_{-\infty}^{t} \epsilon_{i,i+1}(\tau)\,\mathrm{d}\tau. \tag{4.18}$$

Employing these phases it is possible to write an effective Hamiltonian for the two-photon driven saSTIRAP in the form

$$\hat{H}_{\mathrm{eff}} = \frac{\hbar}{2}\begin{bmatrix} 2\epsilon_0(t) & \Omega_{01}(t)\mathrm{e}^{i(\phi_{01}+\tilde{\phi}_{01}(t))} & \Omega_{\mathrm{eff}}(t)\mathrm{e}^{i\tilde{\phi}_{02}(t)} \\ \Omega_{01}(t)\mathrm{e}^{-i(\phi_{01}+\tilde{\phi}_{01}(t))} & 2[\epsilon_1(t)+\delta_{01}] & \Omega_{12}\mathrm{e}^{i(\phi_{12}+\tilde{\phi}_{12}(t))} \\ \Omega^*_{\mathrm{eff}}(t)\mathrm{e}^{-i\tilde{\phi}_{02}(t)} & \Omega_{12}(t)\mathrm{e}^{-(\phi_{12}+i\tilde{\phi}_{12}(t))} & 2[\epsilon_2(t)+\delta_{01}+\delta_{12}] \end{bmatrix}, \tag{4.19}$$

where the added dynamical phases $\tilde{\phi}_{n,n+1}$ cancel the ac-Stark shifts ϵ_n. This can be explicitly seen by applying a unitary transformation

$$\hat{U}_{\phi 2\mathrm{ph}} = \begin{bmatrix} \mathrm{e}^{i\epsilon_0(t)} & 0 & 0 \\ 0 & \mathrm{e}^{i\epsilon_1(t)} & 0 \\ 0 & 0 & \mathrm{e}^{i\epsilon_2(t)} \end{bmatrix} \tag{4.20}$$

to the effective Hamiltonian giving

$$\hat{H'}_{\mathrm{eff}} = \frac{\hbar}{2}\begin{bmatrix} 0 & \Omega_{01}(t)\mathrm{e}^{i\phi_{01}} & \Omega_{\mathrm{eff}}(t) \\ \Omega_{01}(t)\mathrm{e}^{-i\phi_{01}} & 2\delta_{01} & \Omega_{12}\mathrm{e}^{i\phi_{12}} \\ \Omega^*_{\mathrm{eff}}(t) & \Omega_{12}(t)\mathrm{e}^{-i\phi_{12}} & 2(\delta_{01}+\delta_{12}) \end{bmatrix} \tag{4.21}$$

if the time dependence in $\epsilon_n(t)$ is assumed negligible. This Hamiltonian has exactly the correct form for realizing saSTIRAP. In Publication I we have numerically shown that the above results are valid for experimentally feasible parameters and therefore two-photon driving can be used to implement the superadiabatic correction for the STIRAP algorithm.

4.2 Experimental realization of saSTIRAP in a transmon

The saSTIRAP protocol can be realized in a three-level transmon by applying three microwave pulses, where two of them drive the STIRAP part and the third one is used to create the counterdiabatic correction. An important part of the experiment is to be able to maintain the phase coherence between the drives, which is accomplished by using a single microwave source and a high sampling rate arbitrary waveform generator. For details, see Sec. 6.3.

In the experiment the STIRAP pulse shapes are taken as Gaussians given by Eq. (3.18). The shape of the counterdiabatic correction can be calculated from Eq. (4.8) yielding

$$\Omega_{02}(t) = 2\dot{\Theta}(t) = -\frac{t_\mathrm{s}}{\sigma^2}\frac{1}{\cosh\left[\frac{t_\mathrm{s}}{\sigma^2}\left(t - t_s/2\right)\right]} \tag{4.22}$$

if it is assumed that $\Omega_{01} = \Omega_{12}$. In the two-photon driving scheme the pulse shape $\Omega_{02}(t)$ is realized through the effective coupling Ω_eff defined in Eq. (4.14). Therefore the actual pulse shape that needs to be applied to the transmon is $\Omega_\mathrm{2ph}(t) = |\Omega_\mathrm{2ph}(t)|\,\mathrm{e}^{i\phi_\mathrm{2ph}}$, where

$$\begin{aligned} |\Omega_\mathrm{2ph}(t)| &= \sqrt{\left|\frac{2\delta_\mathrm{2ph}}{g}\frac{t_\mathrm{s}}{\sigma^2}\frac{1}{\cosh\left[\frac{t_\mathrm{s}}{\sigma^2}\left(t - t_s/2\right)\right]}\right|}, \\ \phi_\mathrm{2ph}(t) &= \frac{1}{2}\left(\phi_{02} + \tilde{\phi}_{02}(t) - \pi\right) = -\frac{\pi}{4} + \frac{1}{2}\tilde{\phi}_{02}(t). \end{aligned} \tag{4.23}$$

The additional π in the phase comes from the minus sign in the two-photon coupling. The phase $\tilde{\phi}_{02}(t)$ is the dynamical correction resulting from the ac-Stark shifts due to the two-photon driving.

The pulse shapes used to realize saSTIRAP are shown in Fig. 4.1a). Panel b) shows a simulation of the evolution of the state $|2\rangle$ population when three different protocols are applied: a standard STIRAP (blue line), saSTIRAP without dynamical phase correction (red line) and saSTIRAP with the phase correction (yellow line). All the protocols employ Gaussian STIRAP pulses which have equal areas $\mathcal{A} = \int_{-\infty}^{\infty}\Omega_{01}(t)\,\mathrm{d}t = \int_{-\infty}^{\infty}\Omega_{12}(t)\,\mathrm{d}t = 3\pi$. Without the counter-diabatic correction STIRAP leads to $p_2 = 0.95$.

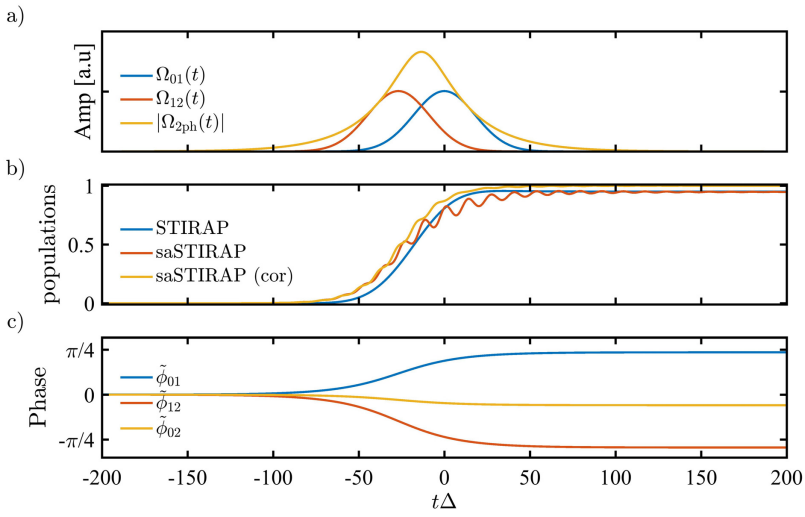

Figure 4.1. a) The pulse envelopes used in saSTIRAP protocol. b) A simulation showing state $|2\rangle$ population p_2 during STIRAP (blue line), saSTIRAP without phase correction (red line) and saSTIRAP with phase correction (yellow line). The areas of the STIRAP pulses are $\mathcal{A}_S = 3\pi$ and their separation is $t_s = 1.5\sigma$. c) The dynamical phase corrections used to cancel the ac-Stark shifts. In the simulation $\lambda = \sqrt{2}$, *i.e* the 1–2 coupling is larger than the 0–1 coupling, which affects the ac-Stark shifts. The time axis is the same in all the plots and it is made unitless by multiplying with the anharmonicity Δ. Figure from Publication I.

The addition of the counterdiabatic pulse seems to lead to higher population in the initial times, but the trajectory starts oscillating, resulting in almost the same population as with STIRAP. This is the consequence of the ac-Stark shifts induced by the two-photon driving, which engenders violation of the phase relation between the pulses, given in Eq. (4.9). By dynamically correcting the phases using Eq. (4.18), the final population of $p_2 = 0.999$ can be reached (yellow line), which demonstrates the importance of the correction. If even higher fidelity in population transfer is required, the phase correction based on the non-degenerate second order perturbation theory is not enough, but degenerate theory should be applied instead. Another option is to increase the pulse width σ, which would lead to smaller two-photon drive amplitude and which would effectively make the energy levels less degenerate. The dynamical phases used to cancel the ac-Stark shifts are shown in Fig. 4.1c).

In Fig. 4.2 the operation of saSTIRAP is demonstrated experimentally. There the measured population p_2 after STIRAP is shown in a) and p_2 after saSTIRAP is shown in b). Each point in the plot corresponds to a parameter pair $(t_\mathrm{s}/\sigma, \sigma)$, which fully characterizes the STIRAP process. In the STIRAP experiment the state $|2\rangle$ population is significantly reduced when the pulse width is too short or the pulse separation is non-ideal. Importantly, saSTIRAP manages to correct the mistake resulting from non-adiabatic excitations, rendering the population transfer uniform across the whole parameter space. The right panels show the corresponding simulations. The solid lines in these panels mark the time it takes to reach the population $p_2 = 0.8$ in each of the points in the parameter space. The transfer times become longer as the pulse width increases, and shorter the larger the pulse separation is. In STIRAP the population transfer takes place during the period when the pulses overlap, and therefore large pulse separation leads to fast but low fidelity population transfer.

4.3 Robustness of the superadiabatic method

Robustness to the noise or errors in external control parameters is one of the main advantages of adiabatic methods. An integral question in the context of superadiabatic methods is whether the robustness associated with adiabatic methods remains. The answer is not obvious, because for example in the case where STIRAP amplitudes are zero, none of the conditions for superadiabaticity are violated. Indeed, in this case perfect

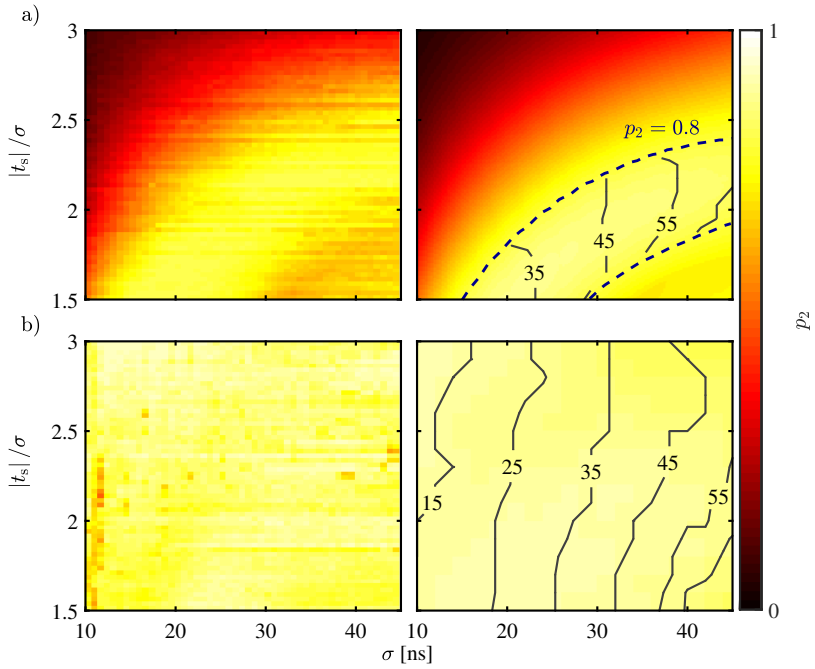

Figure 4.2. a) STIRAP experiment (left panel) and simulation (right) panel as a function of the pulse width σ and normalized pulse separation t_s/σ. b) The corresponding saSTIRAP experiment and simulations. The solid lines denote population transfer times calculated as the duration between the moments when the initial state population drops below $p_0 < 0.99$ and the final state population reaches $p_2 > 0.8$. Figure from Publication III.

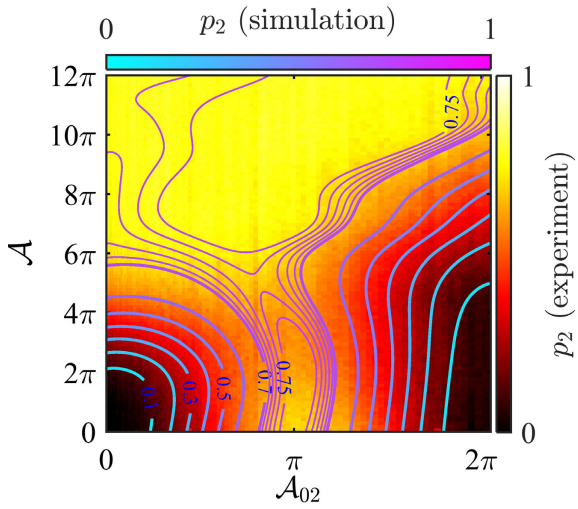

Figure 4.3. Population p_2 as a function of the STIRAP pulse area $\mathcal{A}$ and the counterdiabatic pulse area $\mathcal{A}_{02}$. Figure from Publication III.

population transfer to state $|2\rangle$ is possible, because the counterdiabatic correction has exactly an area equal to π. However, the pulse sequence essentially reduces to an ordinary π pulse and therefore the robustness emerging from adiabaticity is lost. In the other extreme the STIRAP pulse area is practically infinite. In this case the counterdiabatic correction is only a minor perturbation to the otherwise perfect STIRAP and therefore its presence plays no role. Between these two extrema lies the parameter space of practical interest.

Fig. 4.3 shows an experiment demonstrating the amplitude robustness of the saSTIRAP protocol. In the experiment the pulse shapes are kept constant, but their amplitudes are varied. This leads to changes in the pulse areas, which are given by $\mathcal{A} = \int_{-\infty}^{\infty} \sqrt{\Omega_{01}(t)^2 + \Omega_{12}(t)^2}\mathrm{d}t$ for the STIRAP pulses and by $\mathcal{A}_{02} = \int_{-\infty}^{\infty} \Omega_{02}(t)\mathrm{d}t$ for the counterdiabatic correction pulse. When $\mathcal{A} = 0$, the experiment is equal to standard Rabi driving. Consequently, the maximum p_2 is reached when $\mathcal{A}_{02} = \pi$. On the other hand, when $\mathcal{A}_{02} = 0$ the experiment corresponds to pure STIRAP. In this case the population p_2 is a slowly increasing function of the STIRAP area $\mathcal{A}$, which means that the process is robust with respect to its fluctuations, unlike the pure Rabi pulse. The interesting result is observed when both of the areas are non-zero simultaneously, corresponding to saSTIRAP. The presence of the π pulse increases p_2 from the value provided by the STIRAP alone, while the process is simultaneously insensitive to the amplitudes of the pulses. This implies that by using saSTIRAP it is possible

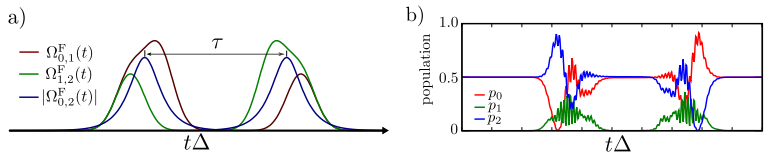

Figure 4.4. a) The pulse sequence used to create the superadiabatic NOT gate consists of two f-STIRAPs (red and green lines) and the counterdiabatic correction (blue line). b) The populations during the NOT-gate. Note that the state $|1\rangle$ population is no longer negligible due to the presence of b-STIRAP. Figure from Publication I.

to reduce the adiabatic losses of STIRAP and to gain robustness to amplitude fluctuations. However, the amount of robustness depends on the area of the STIRAP pulses. From the point of view of robustness the superadiabatic method enables the interpolation between purely adiabatic population transfer and Rabi driving, where the area of the STIRAP part acts as the interpolation parameter.

4.4 Superadiabatic NOT-gate

Typically Hamiltonians used for adiabatic population transfer strictly depend on the initial state $|\psi_{\mathrm{i}}\rangle = |a\rangle$ and the target state $|\psi_{\mathrm{f}}\rangle = |b\rangle$. In order to reverse the process, another Hamiltonian is needed, which prevents the realization of population inversion for an arbitrary initial state. However, bright STIRAP can be used to revoke the condition on the STIRAP pulse order, which also means that the population inversion should work for any initial state in the $\{|0\rangle, |2\rangle\}$ subspace. In Sec 3.1.2 it is shown that b-STIRAP transforms the state $|\psi_{\mathrm{i}}\rangle = \alpha|0\rangle + \beta|2\rangle$ to $\psi_{\mathrm{f}} = \beta|0\rangle - \alpha|2\rangle \mathrm{e}^{i\phi_{\mathrm{f}}}$, where ϕ_{f} is the accumulated phase. The accumulated phase depends on the energy of the bright state $|\mathrm{B}\rangle$, which in turn depends on the STIRAP pulse shapes and the detuning δ. Consequently, even b-STIRAP cannot be directly used as a robust NOT-gate due to the extra phase ϕ_{f}. In [73] it has been shown that the phase can be cancelled by applying a composite pulse that consists of two fractional STIRAPs. The pulse sequence that realizes the composite pulse is given by

$$\begin{aligned} \Omega^{\mathrm{NOT}}_{01}(t) &= \Omega_{01}(t) + \cos(\eta)\Omega_{12}(t) + \sin(\eta)\Omega_{01}(t-\tau), \\ \Omega^{\mathrm{NOT}}_{12}(t) &= \sin(\eta)\Omega_{12}(t) + \Omega_{12}(t-\tau) + \cos(\eta)\Omega_{01}(t-\tau), \end{aligned} \tag{4.24}$$

where τ is the delay between the f-STIRAP sequences and $\eta \in [0, \pi/2]$ is the angle describing the fraction of the population transfer realized

by f-STIRAP, see Sec. 3.1.3. The pulse sequence is shown in Fig. 4.4a) for the case $\eta = \pi/4$. The sequence starts with the initial mixing angle $\tan(\Theta_\mathrm{i}) = \cos(\eta)/\sin(\eta) = \cot(\eta)$, which evolves to $\Theta_\mathrm{int}^{(1)} = \pi/2$ during the first fractional STIRAP because Ω_{12}^F pulse vanishes before Ω_{01}^F pulse. For the second f-STIRAP the initial mixing angle is $\Theta_\mathrm{int}^{(2)} = 0$ because 1–2 pulse starts before 0–1 pulse. During the second f-STIRAP the mixing angle evolves to its final value $\tan(\Theta_\mathrm{f}) = \sin(\eta)/\cos(\eta) = \tan(\eta)$. Using these mixing angles the adiabatic evolution of the initial state $|\psi(-\infty)\rangle = |\psi_\mathrm{i}\rangle = \alpha|0\rangle + \gamma|2\rangle$ can be solved from Eq. (3.10), where the adiabatic eigenstates states are given by Eq. (3.15), yielding the final state

$$|\psi_\mathrm{f}\rangle = \frac{\mathrm{e}^{-i(\phi_\mathrm{f}+\pi/2)}}{\sqrt{2}}\left(i\mathrm{e}^{i(\phi_{01}+\phi_{12})}\gamma|0\rangle - i\mathrm{e}^{-i(\phi_{01}+\phi_{12})}\alpha|2\rangle\right) \tag{4.25}$$

for $\eta = \pi/4$. This corresponds to a unitary transformation

$$U_\mathrm{NOT} = \begin{bmatrix} 0 & \mathrm{e}^{i(\phi_{01}+\phi_{12}+\pi/2)} \\ \mathrm{e}^{-i(\phi_{01}+\phi_{12}+\pi/2)} & 0 \end{bmatrix}, \tag{4.26}$$

which is a NOT-gate with the controllable phase $\phi_{01}+\phi_{12}+\pi/2$. There the common phase factor $\mathrm{e}^{-i(\phi_\mathrm{f}+\pi/2)}$ has been eliminated, which implies that the transformation does not depend the accumulated phase ϕ_f, rendering the gate robust with respect to the amplitudes of the STIRAP pulses. This far the derivation has depended on the assumption of adiabatic evolution. In Publication I we have shown that superadiabatic method can be used to eliminate the diabatic losses of the above NOT-gate, making the adiabatic evolution exact. The superadiabatic method is here especially beneficial, because the adiabatic gate employs b-STIRAP, which operates with single photon detuning. In order to overcome the loss of fidelity due to the reduction in the effective STIRAP pulse area, long pulses would be needed. The superadiabatic method can overcome this limitation by ensuring that diabatic losses do not result in reduction in fidelity.

The superadiabatic correction can be derived by substituting the STIRAP pulse shapes from Eq. (4.24) into the correction Hamiltonian given in Eq. (4.7). The resulting pulse shapes are shown in Fig. 4.4 and the evolution of the state $|\psi(t)\rangle$ during the NOT-gate is shown in 4.4b) for the initial state $|\psi_\mathrm{i}\rangle = \frac{1}{\sqrt{2}}(|0\rangle + |2\rangle)$. There the populations end up being exactly equal in the end of the process due to the perfect NOT-gate provided by the superadiabatic correction.

5. The qubit as a quantum limited magnetometer

Quantum phase estimation is an essential part of many quantum algorithms such as Shor's algorithm [7], and therefore it has been subject to extensive amount of both theoretical and experimental research [74, 75]. In addition to its applications in quantum information processing, phase estimation is important for quantum metrology, where an unknown parameter λ can be determined by measuring the phase $\phi = \Delta E(\lambda)\tau/\hbar$ accumulated during the evolution of the system for the duration τ due to the shift in energy of the system $\Delta E(\lambda)$. In the usual experiments the accuracy of determining the phase is limited by the shot noise, which scales as $\delta\lambda \propto \frac{1}{\sqrt{t}}$, where t is the total time used for sensing the phase. However, ultimately the accuracy is only limited by the Heisenberg relation, yielding the optimal scaling $\delta\lambda \propto \frac{1}{t}$. The Heisenberg limit in the phase estimation can be reached for example by the Kitaev algorithm [76] or using the quantum Fourier transform [77]. Experimentally, these algorithms have been implemented with nitrogen vacancies in diamonds [78].

The modified versions of Kitaev algorithm and quantum Fourier transform can be used for high sensitivity sensing of a magnetic field with a single superconducting qubit. The energy levels of the transmon are very sensitive to the flux piercing its SQUID loop, which makes it an excellent magnetic field detector [79]. By using a Heisenberg-limited algorithm, the sensitivity of the detector can be further improved, which we have demonstrated in Publication II.

The relation of the transition energy of the transmon to the flux piercing the SQUID loop is given by the eigenenergies of the Hamiltonian in Eq. (2.6), $\omega_{01}(\Phi)$. In order to measure the phase accumulated by the flux-dependent energy shift, a Ramsey pulse sequence can be used. There the qubit is first prepared in a superposition state $|\psi\rangle = \alpha|0\rangle + \beta|1\rangle$ by applying a $\pi/2$ pulse at the frequency ω_{01}^{d} and amplitude Ω_{01}. After a

time τ another, $\pi/2$ pulse is applied, whose rotation angle depends on the phase accumulated between the pulses, $\phi = \tau\Delta\omega(\Phi)$, where $\Delta\omega(\Phi) = \omega_{01}(\Phi) - \omega_{01}^{\mathrm{d}}$. After the second pulse the probability to find the qubit in the excited state is given by

$$p_1 = \frac{1}{2} + \frac{1}{2}\mathrm{e}^{-\tau/(T_2)}\gamma(\tau)\cos(\Delta\omega(\Phi)\tau), \tag{5.1}$$

which reveals the Ramsey oscillations [80] as function of the delay between the pulses or the detuning $\Delta\omega(\Phi)$ (Fig. 5.1a)). Here it is assumed that the drive amplitude satisfies $\Omega_{01} \gg \Delta\omega(\Phi)$ so that the amplitude of the oscillations is not reduced due to the detuning. The oscillations decay in time with the time constant $T_2 = 1/(\frac{1}{2T_1} + \frac{1}{T_\phi})$ where T_1 is the energy relaxation rate of the qubit and T_ϕ is the pure dephasing rate. In addition to the exponential decay with τ in the first order, there can also be a contribution from colored noise described by $\gamma(\tau) = \mathrm{e}^{-(\tau^2/T_\phi^{(2)} + \tau^3/T_\phi^{(3)} + \ldots)}$ [81], but here their contribution can be neglected due to the dominance of the dephasing due to the energy relaxation in the sample.

In the standard quantum experiment the magnetic flux can be estimated by measuring p_1 at some given delay τ_0. As long as the response function p_1 is single valued over the whole range of possible flux values (i.e. $0 \geq \Delta\omega(\Phi)\tau \geq \pi$), the flux can be uniquely determined by repeating the Ramsey experiment several times.

The accuracy of the estimation can be calculated using the mean squared error $\mathrm{MSE}(\hat{p}_1) = \mathbb{E}\left[(\hat{p}_1 - p_1)^2\right]$, where $\hat{p}_1$ is the estimator for the probability p_1. In case of a projective measurement, the measurement outcomes follow a binary distribution with the probability p_1 of measuring the excited state. For N repeated measurements the estimator $\hat{p}_1 = N_1/N$, where N_1 is the number of experiments giving the excited state as a result. The MSE can then be written as $\mathrm{MSE}(\hat{p}_1) = \mathbb{E}\left[\frac{N_1^2}{N^2} - \frac{2N_1 p_1}{N} + p_1^2\right] = \frac{p(1-p)}{N}$, where the variance $\mathbb{E}[N_1^2] - \mathbb{E}[N_1]^2 = Np_1(1-p_1)$ and the mean $\mathbb{E}[N_1] = Np_1$ of the binomial distribution have been used. The largest squared error is given for $p_1 = 1/2$, yielding $\mathrm{MSE}(\hat{p}_1) = \frac{1}{4N}$. Consequently, the error of the estimate drops as $\delta p_1 = \sqrt{\mathrm{MSE}(\hat{p}_1)} = \frac{1}{2\sqrt{N}}$, which is the standard quantum limit. The error in estimating the flux can be then derived as

$$\delta\Phi = \left|\frac{\partial p_1}{\partial\Delta\omega(\Phi)}\frac{\partial\Delta\omega(\Phi)}{\partial\Phi}\right|^{-1}\delta p_1 = \left|\frac{\partial\Delta\omega(\Phi)}{\partial\Phi}\right|^{-1}\frac{\mathrm{e}^{\frac{\tau}{2T_1}}}{\tau\sqrt{N}}, \tag{5.2}$$

where the factor $\sin(\Delta\omega(\Phi)\tau)$, resulting from the differentiation of the cosine in Eq. (5.1), is taken as 1 for simplicity. The approximation might lead to underestimation of the error, but in the experimental realization

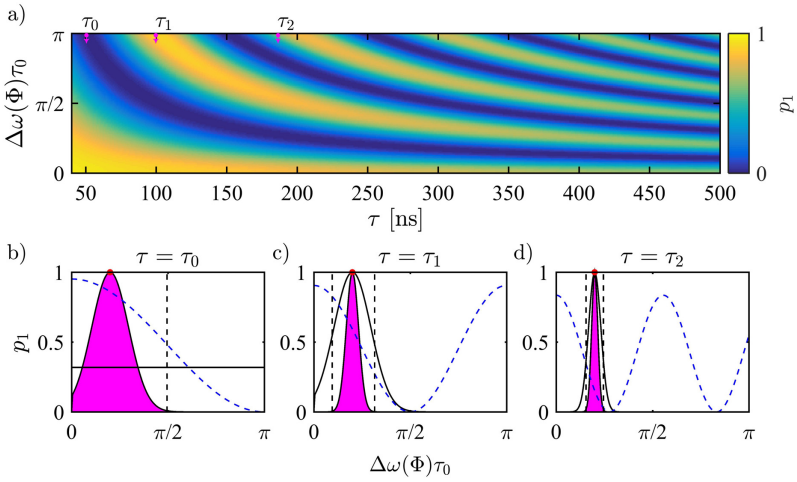

Figure 5.1. a) The probability to measure the excited state as a function of the delay between the Ramsey pulses τ and the detuning $\Delta\omega(\Phi)$ normalized with $\tau_0 = 50$ ns. b) The illustrations shows the progress of the modified Kitaev algorithm. Initially the normalized detuning $\Delta\omega(\Phi)\tau_0$ generated by the flux through the transmon loop is unknown, which is described by the flat probability distribution (black line). After a few repetitions of the experiment some information is gathered, resulting in the narrowing of the probability distribution (magenta) around the actual value of the flux (red dot). The dashed blue line shows the cross-section of the response function given in a), measured at $\tau = \tau_0$. The shown probability distributions are not normalized. c) Due to the narrowing of the probability distribution it is possible to rule out some of the flux values, which enables changing τ from τ_0 to τ_1 thus increasing the accuracy of the estimation while the response curve is still single-valued for all the flux values for which the probability is higher than some small parameter ϵ_K. d) After additional repetitions of the experiment at $\tau = \tau_1$, τ can be further increased to τ_2. New steps can be taken until $\tau = T_2$.

of the Kitaev algorithm the measurement time τ can be optimized so that the estimate is valid. However, in the standard measurement scheme τ needs to be taken as short as possible in order to maximize the range of fluxes which can be uniquely determined, resulting in $\delta\Phi \propto \frac{1}{\sqrt{N}} \propto \frac{1}{\sqrt{t}}$, where the total measurement time is defined as $t = N(\tau + \tau_{\text{overhead}})$. The power of the quantum algorithms is based on accumulating the phase over large values of τ instead of repeating the experiment, in which case $\delta\Phi \propto \frac{1}{t}$, if τ_{overhead} is assumed zero. However, due to the exponential decoherence term in Eq. (5.2), the reduction in flux error is saturated at $\tau = T_2$. After this limit the error can be further reduced by averaging, but the reduction only follows the standard quantum limit. Here the task of the quantum phase detection algorithm is to reach the optimal measurement time while still being able to distinguish all the flux values from each other.

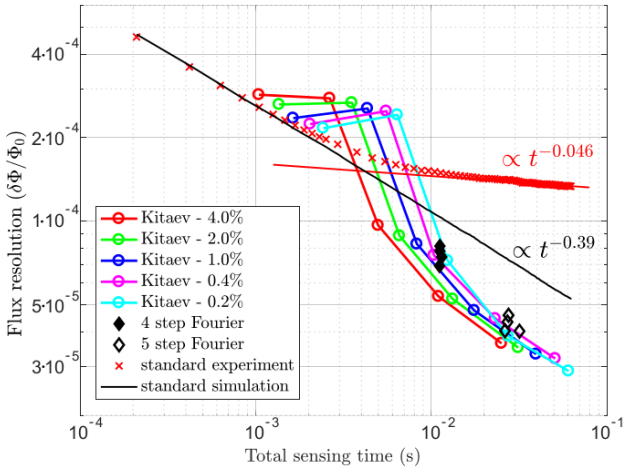

Figure 5.2. The experimental resolution at which flux is determined as a function of the total sensing time. The lines with circles show the resolution achieved with the modified Kitaev algorithm with different allowed error rates ϵ_K at each step. During the algorithm the resolution was measured at every value of τ applied. The experiment shows that initially the Kitaev algorithm provides a significant speed-up over the shot-noise-limited standard experiment (red crosses). However, after a few steps the speedup reduces to the shot-noise limit because $\tau \approx T_2$ is reached. Figure from Publication II.

In the Kitaev algorithm the Heisenberg limit is reached by gradually eliminating the most unlikely flux values, which limits the range of possible fluxes. This allows one to increase τ without violating the condition of unique response for each flux value. If half of the flux values are eliminated at each step, then ideally τ can be incremented as $\tau_{n+1} = 2\tau_n$. Experimentally τ is chosen to give the maximal difference between the responses, which can lead to small deviations from the ideal values. Fig. 5.1 demonstrates the operation of the modified Kitaev algorithm. In Publication II we have experimentally realized the modified Kitaev algorithm and demonstrated the speedup over the shot-noise limited case. The results of the experiment are shown in Fig. 5.2, where the achieved flux resolutions are shown as a function of the time used in measuring the flux. After the first step the resolution increases dramatically but it soon saturates to the shot-noise limited case due to the decoherence. The experiments were performed using a sample with $T_2 = 260$ ns, which allows for approximately 4 steps in the Kitaev algorithm. However, even the few steps with the Heisenberg-limited scaling are enough to result in an order of magnitude increase in the flux resolution over the standard measurement.

6. Experimental and numerical methods

6.1 Numerical solution to the time evolution of the system

The time evolution of the transmon can be numerically found using the Schrödinger equation $|\dot{\psi}(t)\rangle = -\frac{i}{\hbar}\hat{H}|\psi(t)\rangle$, which describes a system of coupled linear differential equations. As long as the number of simulated energy levels is not excessively large, the state $|\psi(t)\rangle$ can be solved efficiently by using the implicit Runge-Kutta method with adaptive step size.

The coupling of the system with its environment leads to decoherence, which can be modelled as a weak interaction with a bath of harmonic oscillators. If the correlations of the state of the bath with the system state vanish quickly when compared to all the other time scales of the system (the Markovian approximation), the reduced dynamics of the transmon and the resonator can be solved from the Lindblad equation [82]

$$z\dot{\hat{\rho}}(t) = -\frac{i}{\hbar}\left[\hat{H}, \hat{\rho}(t)\right] + \sum_i \gamma_i \left[\hat{L}_i \rho(t) \hat{L}_i^\dagger - \frac{1}{2}\left(\hat{L}_i^\dagger \hat{L}_i \hat{\rho}(t) + \hat{\rho}(t)\hat{L}_i^\dagger \hat{L}_i\right)\right], \quad (6.1)$$

where γ_i is the coupling coefficient with the bath, $\hat{L}_i$ is the coupling operator and $\hat{\rho}(t)$ is the density matrix of the system. The energy relaxation of the three-level transmon is modelled with the operators $\hat{L}_0 = |0\rangle\langle 1|$ and $\hat{L}_1 = |1\rangle\langle 2|$ and the corresponding relaxation rates $\gamma_0 = \Gamma_{01}$ and $\gamma_1 = \Gamma_{12}$ [83]. In addition to the energy relaxation there can also be energy conserving virtual processes that result in pure dephasing of the transmon. The pure dephasing can be caused by the fluctuations in the energy levels of the transmon due to the flux noise or by the virtual transitions between the transmon and its environment [83]. The dephasing can be modelled with the the operators $\hat{L}_2 = |1\rangle\langle 1|$, $\hat{L}_3 = |2\rangle\langle 2|$ and the rates $\gamma_2 = \Gamma_1^\phi$, $\gamma_3 = \Gamma_2^\phi$ if the noise on the 0–1 and 1–2 transitions is assumed to be inde-

pendent.

By design, the resonator couples to the environment through the input capacitor with the relaxation rate κ and the operator $\hat{L}_4 = \hat{a}$, which allows for the readout photons to leak out. In addition to the engineered relaxation, there are also internal losses in the resonator, but here they are neglected due to their vanishing contribution. With these terms the Lindblad equation becomes

$$\begin{aligned}\dot{\hat{\rho}}(t) = &-\frac{i}{\hbar}\left[\hat{H}_{\mathrm{JC}}, \hat{\rho}(t)\right] + \Gamma_{01}\left(\sigma_{01}\hat{\rho}(t)\sigma_{10} - \frac{1}{2}\left(\sigma_{11}\hat{\rho}(t) + \hat{\rho}(t)\sigma_{11}\right)\right), \\ &+ \Gamma_{12}\left(\sigma_{12}\hat{\rho}(t)\sigma_{21} - \frac{1}{2}\left(\sigma_{22}\hat{\rho}(t) + \hat{\rho}(t)\sigma_{22}\right)\right), \\ &+ \Gamma_1^{\phi}\left(\sigma_{11}\hat{\rho}(t)\sigma_{11} - \frac{1}{2}\left(\sigma_{11}\hat{\rho}(t) + \hat{\rho}(t)\sigma_{11}\right)\right), \\ &+ \Gamma_2^{\phi}\left(\sigma_{22}\hat{\rho}(t)\sigma_{22} - \frac{1}{2}\left(\sigma_{22}\hat{\rho}(t) + \hat{\rho}(t)\sigma_{22}\right)\right).\end{aligned} \tag{6.2}$$

If one only wants to simulate the evolution of the transmon in the absence of the resonator, the dispersive contribution of the resonator can be included as small shifts in the transmon frequencies, as is done in Sec. 3.1. Due to the dispersive coupling the transmon slowly relaxes through the resonator, which is characterized by the Purcell decay rates [84, 85] $\gamma_i^{\mathrm{p}} = \kappa\frac{g_{i,i+1}^2}{\Delta_i^2}$ for the i:th state. In the reduced space the coefficients $\Gamma_{01} \to \Gamma_{01}+\gamma_0^{\mathrm{p}}$ and $\Gamma_{12} \to \Gamma_{12}+\gamma_1^{\mathrm{p}}$ can be updated to take that into account.

6.2 Experimental methods

The experiments presented in this thesis were carried out using three different transmon samples with 0–1 transition frequencies ranging from 5 GHz to 8 GHz. The transmons were coupled to quarter-wave resonators with resonance frequencies ranging from 4 GHz to 5.5 GHz.

The samples are cooled down using a BlueFors BF-LD250 helium dilution refrigerator with the base temperature of 15 mK. The cryostat is divided into several different temperature stages, with the consecutive stages having lower and lower temperatures. The samples are attached to a flange connected to the lowest temperature stage, which is directly cooled down by the dilution process in the mixing chamber.

There are two control lines connected to the sample, one high-frequency line capacitively coupled to the gate electrode of the transmon and one dc-line used to apply a constant flux through the transmon loop, shown in Fig. 6.1. In addition, there are input and output lines used for the

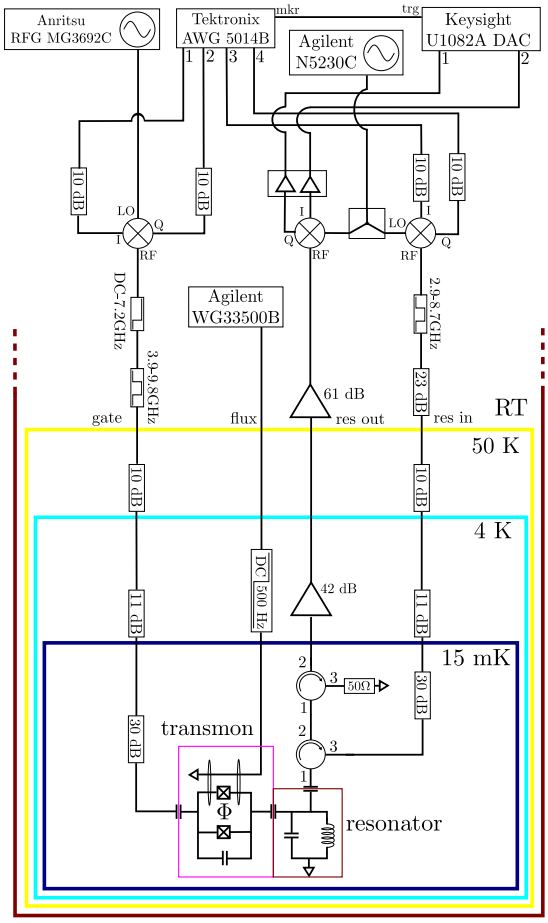

Figure 6.1. The experimental setup used in Publication III. A similar setup has also been used in other publications with small variations. The figure shows the wiring in different temperature stages in the cryostat as well as the room temperature electronics used to create the control and the readout pulses.

readout, which are connected to the microwave resonator through two circulators, which separate the in-going and out-going signals.

The input lines are attenuated so that the thermal noise from the room temperature cannot enter the sample. The noise temperature (the amount of added noise, measured in units of temperature) of an attenuator chain can be evaluated recursively from

$$T_{i-1}^{\mathrm{N}} = T_{i-1} + (T_i^{\mathrm{N}} - T_{i-1})/A_{i-1}, \tag{6.3}$$

where T_{i-1} is the temperature of the attenuator and T_i^{N} is the thermal noise at the input of the attenuator. The difference $T_i^{\mathrm{N}} - T_{i-1}$ gives the amount of noise which the higher temperature stage would generate if no

attenuation were used. In order to prevent the thermal noise from exciting either the transmon or the resonator, the noise temperature at the sample needs to be much smaller than 200 mK, which can be estimated from Wien's approximation $B(f) \propto \mathrm{e}^{-\frac{hf}{k_\mathrm{B}T}}$. Assuming that the sample temperature of 50 mK is sufficient, the attenuation required to protect the sample from the thermal noise is $A_0 \gg 48$ dB. However, the attenuated part of the signal is radiated as heat, which prevents all the attenuation from being installed in the lowest temperature stage, because the cooling power of the cryostat is the smallest there. Therefore an attenuator chain is formed which distributes the generated heat more evenly between the different temperature stages. Using the attenuation and temperature values given in Fig. 6.1 the noise temperature seen by the sample through the gate line is given by Eq. (6.3) as $T_0^\mathrm{N} = 25$ mK. In reality the temperature of the sample might be slightly higher due to its imperfect thermalization to the cryostat body.

A similar attenuator chain is installed in the input line of the resonator. In the output line of the resonator an amplifier chain is used to multiply the tiny flow of photons leaking from the resonator. The noise temperature of the amplifier chain can be evaluated from

$$T_i^\mathrm{N} = T_i + T_i^\mathrm{amp} + T_{i+1}^\mathrm{N}/G_i, \tag{6.4}$$

where T_i^amp is the noise temperature of the amplifier, T_i is the temperature of the environment and G_i is the amplification of the amplifier. The low temperature amplifier LNF-LNC4-8A used in the readout line has noise temperature of 3 K and gain of 42 dB, which gives the total noise temperature of 7 K in the end of the amplifier chain. Here the contribution from the room temperature amplifiers noise is negligible because of the huge amplification of the low temperature amplifier. The role of the room temperature amplifiers is to adjust the signal level to be appropriate for the analog-to-digital converter (Keysight U1082A) recording the signal.

The flux line is filtered using an RC filter with the cutoff frequency at 500 Hz. The heavy filtering prevents any fast modifications of the energy levels of the transmon, but also stops the high frequency noise from dephasing the transmon. The 3.5 kΩ resistance of the filter also attenuates the thermal noise at DC.

6.3 Pulse synthesis

The pulses used to control the transmon are created by an arbitrary waveform generator Tektronix AWG 5014B. The maximum sampling rate of the AWG is 1.2 GS/s, which means that directly outputting signals that drive the transmon is not possible (the 0–1 transition frequency of the transmon is in range of 5 - 8 GHz). Therefore the pulse envelopes created by the AWG are upconverted using an IQ-mixer (Marki IQ-0307L) and a signal generator (Anritsu MG3692C for the gate and Agilent 5230C for the resonator) providing the carrier signal. A schematic of an IQ-mixer is shown in Fig. 6.2a). As opposed to a standard mixer, the IQ-mixer provides two ports for the intermediate frequency (IF) which have a $\pi/2$ phase shift between them, allowing for more control over the output signal. Similarly to a standard mixer, the IQ-mixer can be either used for up- or down-conversion. In upconversion the target signal can be applied either to I or Q channel, which are mixed with the local oscillator (LO) signal resulting in

$$s_{\mathrm{uc}}(t) = \kappa_{\mathrm{uc}} \left[I(t) \sin(2\pi f_{\mathrm{LO}} t + \phi_{\mathrm{LO}}) + Q(t) \cos(2\pi f_{\mathrm{LO}} t + \phi_{\mathrm{LO}}) \right] \tag{6.5}$$

at the RF port. Here κ_{uc} is the conversion loss of the mixer and the wave $A_{\mathrm{L}} \sin(2\pi f_{\mathrm{L0}} t + \phi_{\mathrm{LO}})$ is provided from the LO port. In the downconversion the signal in the RF port is mixed with the local oscillator signal and the resulting quadratures appear in the I and Q ports,

$$\begin{aligned} I_{\mathrm{dc}}(t) =& \kappa_{\mathrm{dc}} s(t) \cos(2\pi(f_{\mathrm{RF}} - f_{\mathrm{LO}})t + \phi_{\mathrm{RF}}(t) - \phi_{\mathrm{LO}}), \\ Q_{\mathrm{dc}}(t) =& \kappa_{\mathrm{dc}} s(t) \sin(2\pi(f_{\mathrm{RF}} - f_{\mathrm{LO}})t + \phi_{\mathrm{RF}}(t) - \phi_{\mathrm{LO}}). \end{aligned} \tag{6.6}$$

I and Q can be interpreted as the Cartesian representation of the signal amplitude $s(t)$ and the phase $\phi_{\mathrm{RF}}(t)$ and thus any wave with arbitrary amplitude and phase can be decomposed into its I and Q components, see Fig. 6.2b).

Analog mixers have several deficiencies such as lack of isolation between the channels. The leakage of the local oscillator (LO) signal to the RF port can cause a significant reduction in the gate fidelities. Typically the signal generator providing the LO signal is continuously on, but ideally no signal is generated in the RF port because the IF amplitude is zero. However, if there is LO leakage the transmon is constantly driven, creating excitations. The LO leakage can be suppressed by applying constant offsets into the I and Q ports of the IQ-mixer, which creates a waveform that cancels the leakage [86]. The cancellation is possible due to the $\pi/2$ phase

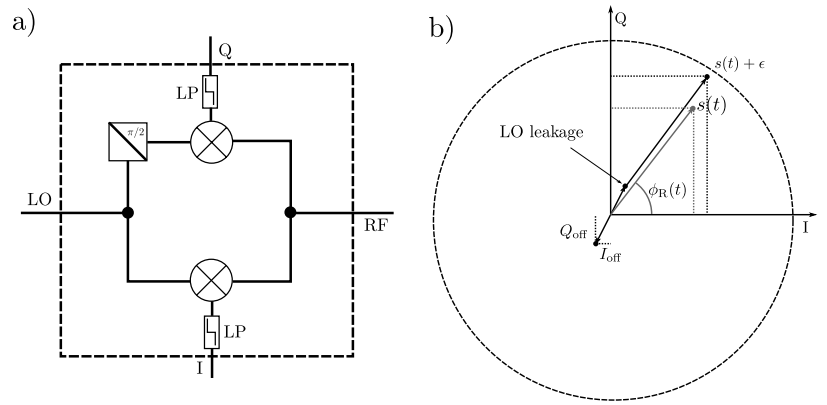

Figure 6.2. a) An IQ-mixer consists of two balanced paths with a $\pi/2$ phase shift between the them. In both paths there is a frequency mixer, which mixes the signals appearing in the RF port and in the LO port, resulting in signals at the intermediate frequency $f_{\mathrm{RF}} - f_{\mathrm{LO}}$ in I and Q ports. In addition, the mixers produce a high frequency component $f_{\mathrm{LO}} + f_{\mathrm{RF}}$, which is removed by the low-pass filters after the mixers. b) Representation of a signal with amplitude $s(t)$ and phase $\phi_{\mathrm{R}}(t)$ in the IQ-plane. The LO-leakage adds an additional vector component to the signal, which can be cancelled with the constant offsets I_{off} and Q_{off}.

difference of I and Q channels which allows a compensation signal with arbitrary phase to be created, resulting in almost perfect cancellation. In practice the voltages needed for the correction vary between different mixers and LO frequencies, and therefore the offsets need to be found separately for each piece. In addition, the parameters may vary in time due to changes in the temperature and humidity. Typically the offset corrections are a few millivolts, but can be as high as 20 mV.

Another way to avoid the LO leakage is to modulate the pulse envelope with an intermediate frequency, $I(t) = A(t)\sin(2\pi f_{\mathrm{IF}} t + \phi_{\mathrm{I}})$. As a result, the mixer creates signals at frequencies $f_{\mathrm{LO}} + IF$ and $f_{\mathrm{LO}} - IF$. By setting $f_{\mathrm{LO}} - IF \approx f_{01}$ the leakage at f_{LO} is off-resonant from the transition frequency f_{01} and the envelope seen by the transmon is given by $A(t)$. In this case the mirror signal at $f_{\mathrm{LO+IF}}$ can create errors, for example by driving higher transitions. It is possible to operate the IQ-mixer as a single side band (SSB) mixer by manipulating the I and Q components. By applying a phase-shifted signal $Q(t) = A(t)\sin[2\pi f_{\mathrm{IF}} t + \phi_{\mathrm{I}} + \pi/2]$ into the Q port, from Eq. (6.5) the resulting signal can be calculated as $s_{\mathrm{SSB}}(t) = \kappa_{\mathrm{uc}} A(t)\cos[2\pi(f_{\mathrm{IF}} - f_{\mathrm{LO}})t + \phi_{\mathrm{I}} - \phi_{\mathrm{LO}}]$, where the upper side band has been eliminated. Applying a phase shift of $-\pi/2$ instead would result in elimination of the lower side band. In analog mixers the two paths of the mixer are never completely equal, resulting in amplitude imbalance

between the channels. There are also deviations from the ideal interchannel phase difference of $\pi/2$. These deviations impair the quality of SSB mixing if not taken into account properly. In case I and Q signals are created digitally, it is possible to apply amplitude and phase correction factors directly to the waveforms, which cancel the errors of the mixer. Consequently, the corrected I and Q signals are

$$\begin{aligned} I(t) &= A(t)\sin(2\pi f_{\mathrm{IF}} t + \phi_{\mathrm{I}}) + I_{\mathrm{off}}, \\ Q(t) &= (A(t) + A_\epsilon)\sin(2\pi f_{\mathrm{IF}} t + \phi_{\mathrm{I}} + \pi/2 + \phi_\epsilon) + Q_{\mathrm{off}}, \end{aligned} \tag{6.7}$$

where the correction parameters I_{off}, Q_{off}, A_ϵ, and ϕ_ϵ can be manually determined by using a spectrum analyzer and test waveforms with constant amplitudes on I and Q channels. When the offsets are tuned correctly, the signal at LO frequency disappears. Similarly, the spurious sideband disappears when the amplitude and phase correction coefficients are set correctly.

By applying SSB mixing it is possible to combine signals acting on different transmon transitions into a single pulse. This guarantees the phase coherence between the signals as the different frequency components are digitally created using the same channels of the arbitrary waveform generator. The applicability of the method is limited by the sampling rate of the arbitrary waveform generator which has to be more than twice larger than the difference in the driven transition frequencies due to the Nyquist criterion. In addition, the IQ-mixers have a limited bandwidth which results from the cutoff frequency of their low-pass filters. In the experiments presented in this thesis these criteria were satisfied as Tektronix AWG5014B has the sampling rate of 1.2 GS/s, which is large when compared to the anharmonicity of the used transmons (less than 400 MHz for all the samples). The bandwidth of IQ-0307L mixers is 500 MHz which is also appropriate. When driving a three-level system the requirement for the high sampling rate can be reduced by a factor of two by setting the LO frequency to $f_{\mathrm{LO}} \approx (f_{01} + f_{12})/2$ and employing the upper and lower side bands for the 0–1 and 1–2 transitions. However, in this case it is advisable to add a small detuning from the frequency $(f_{01} + f_{12})/2$ to avoid the LO leakage to the two-photon 0–2 transition and to minimize the errors from the mistakes in the calibration of SSB mixing; without the detuning, the mistakes would result in resonant driving of the wrong transition.

6.4 Measurement of the occupation probabilities in a three-level system

The readout of the transmon state is based on the dispersive shift of the resonator transition frequency [87]. The resonator transition frequency is probed by sending a microwave pulse through the input line and measuring the reflected signal, directed into the output line by the circulators. If the probe signal is in resonance with the resonator, the reflected signal is reduced due to the resonator absorbing some of the photons.

The probe pulse is produced by the Tektronix 5014B arbitrary waveform generator which is also used to synthesize the gate pulses. The rectangular I and Q envelopes are mixed in an IQ-mixer with an LO signal derived from the Agilent N5230C network analyzer acting as a signal generator, resulting in a rectangular pulse at the probe frequency ω_p. The reflected signal is amplified by the amplifier chain and lead to another IQ-mixer, which shares the LO with the input mixer, ensuring phase stability between the in-going and out-going signals. The input mixer acts as a demodulator, down-converting the incoming RF-signal back to DC. After amplification by Stanford Research Systems SR445A preamplifier, the signal is digitized by the Keysight U1082A analog-to-digital converter, which can calculate averaged responses of up to 65000 realizations of the experiment. The measured averaged voltages can be linked to the creation and the annihilation operators of the transmission line as

$$\langle \hat{V}_\mathrm{tr}(t)\rangle = -\left\langle \int \hat{E}(s,t)\mathrm{d}s \right\rangle = iv\left(\langle \hat{b}_\mathrm{out}(t)\rangle \mathrm{e}^{i\omega_\mathrm{p}t} - \langle \hat{b}^\dagger_\mathrm{out}(t)\rangle \mathrm{e}^{-i\omega_\mathrm{p}t}\right), \tag{6.8}$$

where $\hat{E}(s,t)$ is the electric field in the transmission line, ω_p is the probe frequency, v is a prefactor containing all the constants, $\langle \hat{b}_\mathrm{out}(t)\rangle = \mathrm{Tr}(\hat{b}_\mathrm{out}\rho(t))$ is the averaged annihilation operator of the resonator and $\rho(t)$ is the density matrix describing the state of the system. According to the input/output formalism [88] the field coming from the resonator $\hat{b}_\mathrm{out}(t)$ can be written in terms of the input field $\hat{b}_\mathrm{in}(t)$ and the resonator field as

$$\langle \hat{b}_\mathrm{out}(t)\rangle = \langle \hat{b}_\mathrm{in}(t)\rangle + \sqrt{\kappa}\langle \hat{a}(t)\rangle, \tag{6.9}$$

where κ is the rate at which the photons leak out of the resonator through the input capacitor. The output field is demodulated in the IQ-mixer with the local oscillator signal given by $\hat{V}_\mathrm{LO}(t) = A_\mathrm{LO}\left(\hat{c}\mathrm{e}^{i(\omega_\mathrm{p}t+\phi_\mathrm{LO})} + \hat{c}^\dagger \mathrm{e}^{-i(\omega_\mathrm{p}t+\phi_\mathrm{LO})}\right)$,

which transforms the field in to quadratures

$$\begin{aligned}\langle\hat{I}(t)\rangle =& v_{\mathrm{IQ}}\left[\langle\hat{b}_{\mathrm{in}}^{\dagger}(t)\rangle e^{i\phi_{\mathrm{LO}}}+\langle\hat{b}_{\mathrm{in}}(t)\rangle e^{-i\phi_{\mathrm{LO}}}+\sqrt{\kappa}\left(\langle\hat{a}^{\dagger}(t)\rangle e^{i\phi_{\mathrm{LO}}}+\langle\hat{a}(t)\rangle e^{-i\phi_{\mathrm{LO}}}\right)\right],\\ \langle\hat{Q}(t)\rangle =& iv_{\mathrm{IQ}}\left[\langle\hat{b}_{\mathrm{in}}^{\dagger}(t)\rangle e^{i\phi_{\mathrm{LO}}}-\langle\hat{b}_{\mathrm{in}}(t)\rangle e^{-i\phi_{\mathrm{LO}}}+\sqrt{\kappa}\left(\langle\hat{a}^{\dagger}(t)\rangle e^{i\phi_{\mathrm{LO}}}-\langle\hat{a}(t)\rangle e^{-i\phi_{\mathrm{LO}}}\right)\right],\end{aligned} \tag{6.10}$$

where it has been assumed that the local oscillator signal is classical so that $\langle\hat{c}\rangle \approx \langle\hat{c}^{\dagger}\rangle$ and it can be included in the prefactor v_{IQ} along with all the other constants. Both quadratures consist of the transmon state independent part and the actual state dependent response. The response function that includes the information of the both quadratures can be simply written as a column vector $r_{\mathrm{m}}(t) = \{\langle\hat{I}(t)\rangle, \langle\hat{Q}(t)\rangle\}^{\mathrm{T}}$, where t takes discrete values due to the digitization. If it is assumed that the measurement quickly dephases the transmon producing a mixed state, the response of an arbitrary state can be written as a linear combination

$$r_{\mathrm{m}}(t) = \sum_i p_i r_i(t) \tag{6.11}$$

where $r_i(t)$ are the responses of the system in state $|i\rangle$ and p_i are real factors for which $\sum_i p_i = 1$. The constraint allows the elimination of one of the degrees of freedom, resulting in $r'_{\mathrm{m}}(t) = r_{\mathrm{m}} - r_0 = \sum_{i=1} p_i(r_i(t) - r_0(t))$. This way the occupation probabilities p_0 and $p_1 = 1 - p_0$ for the two-level system can be calculated as

$$p_1 = \frac{\int_{t_0}^{t_1}(r_{\mathrm{m}}(t) - r_0(t))\mathrm{sgn}(r_1(t) - r_0(t))\mathrm{d}t}{\int_{t_0}^{t_1}(r_1(t) - r_0(t))\mathrm{sgn}(r_1(t) - r_0(t))\mathrm{d}t}, \tag{6.12}$$

where $\mathrm{sgn}(r_1(t) - r_0(t))$ ensures that the possibly oscillating positive and negative parts of the signals add up. Note that the part of the measurement responses which is independent of the transmon state is cancelled due to the constraint on the populations.

The populations of multi-level systems cannot be solved in a single averaged measurement using the integration method presented above because the parameter space is no longer one dimensional. Following the method introduced in [38], the populations of the states can be extracted by fitting the measured trajectory to the calibration responses of the known states. The problem can be formulated as system of linear equations $r'_{\mathrm{m}} = Rp$, where R is a system matrix whose columns contain the responses $r_i - r_0$ and p is a column vector of the populations $\{p_1, p_2, ...\}^{\mathrm{T}}$. Finding the populations is an inverse problem, for which the least squares solution can be achieved using the Moore-Penrose pseudoinverse $R^{+} = (R^{\mathrm{T}}R)^{-1}R^{\mathrm{T}}$ [89] if R consists of linearly independent real vectors, yielding the populations

$p = R^{+} r'_{\mathrm{m}}$. If the calibration responses are linearly dependent, the system matrix becomes ill-conditioned, which results in statistical fluctuations in the inferred populations. The effect of the fluctuations can be analyzed from the covariance matrix of the populations, $\Sigma = \mathbb{E}[(p - \mathbb{E}[p])(p - \mathbb{E}[p])^{\mathrm{T}}]$, where the noise is simulated by adding a Gaussian distributed random vector with zero mean into the measured trajectory, $s_{\mathrm{m}} = r'_{\mathrm{m}} + \epsilon$. By substituting the expression for the noisy populations $p = R^{+} r'_{\mathrm{m}} + R^{+}\epsilon$ into the covariance matrix, it can be written as

$$\Sigma = \sigma_{\epsilon}^{2} (R^{\mathrm{T}} R)^{-1}, \tag{6.13}$$

where σ_{ϵ}^{2} is the variance of the noise vector ϵ. Clearly, if any of the eigenvalues of the normal matrix $R^{\mathrm{T}} R$ is close to zero, the corresponding diagonal element in the covariance matrix is very large, indicating that the measurement is noisy. The singularities in the normal matrix can be avoided if all the calibration trajectories are linearly independent, which is characterized by the determinant $\det G = \det (R^{\mathrm{T}} R) = \prod_i \lambda_i$ [90], where λ_i are the eigenvalues of the normal matrix. In practice the readout can be optimized by sweeping the measurement pulse amplitude A_{p} and its frequency ω_{p} to find the maximal determinant of the normal matrix which ensures that the variances of the populations are small on average. Fig. 6.3a) shows an example of such an experiment along with the measurement responses corresponding to an optimal point shown in Fig. 6.3b).

The determinant of the normal matrix is not the only possible measure for the optimal readout. Another option would be to use the condition number of the system matrix as the optimization criterion, $\kappa_{\mathrm{C}}(R) = \lambda_{\max}/\lambda_{\min}$, where $\lambda_{\min}$ and $\lambda_{\max}$ are the largest and the smallest singular values of the matrix R [91]. The condition number describes the sensitivity of the result to small changes in the input data, such as noise in the measurement responses. Large values indicate that the matrix is ill-conditioned. However, the determinant of the normal matrix was favoured as the optimization metric because it ensures that the uncerainty in the populations is evenly distributed between the different states. This is important in the experiments, where all the states can be populated.

The method based on solving the inversion problem is a powerful tool because the populations of all the states can be found in a single averaged experiment, which has been applied in Publication III and Publication VI. The drawback of the method is that the responses of the basis states are linearly independent mostly during the resonator transient time, which

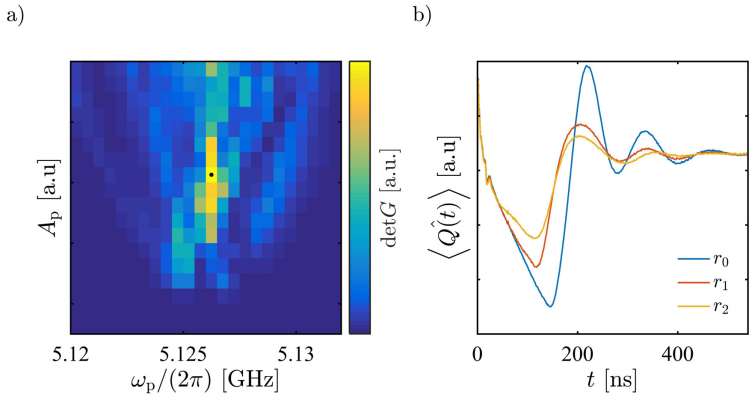

Figure 6.3. a) The Gram determinant of the measurement responses as a function of the probe frequency ω_p and the probe pulse amplitude A_p. The black dot shows the optimal measurement point. b) The Q-part of the measurement responses corresponding to the transmon in states $|0\rangle$, $|1\rangle$ and $|2\rangle$ in the optimal measurement point.

limits the duration of the measurement to timescales $t_\mathrm{m} \sim 1/\kappa$ and therefore limits the measurement fidelity.

7. Conclusions

Circuit quantum electrodynamics is an ideal testbed for studying advanced quantum control protocols. The samples have well known characteristics and are well described by relatively simple theoretical models. This allows for accurate simulations of the experimental results which further enables precise confirmation of the theoretical predictions. This prolific cycle is a textbook example of the scientific method, where theory and experiments support each other producing repeatable results with growing complexity.

In this thesis I have employed a transmon circuit to realize several experiments that demonstrate adiabatic control of a three-level quantum system. In Publication VI the stimulated Raman adiabatic passage method was used to excite the transmon to the second excited state. The method originates from the quantum control of molecular states, but our experiment demonstrates for the first time that the method is also valid in circuit quantum electrodynamics. The method's most important feature is the insensitivity to the control parameters, which enables robust quantum state control. In Publication IV I have theoretically investigated additional limitations in the method which arise from the low anharmonicity of the transmon. Stimulated Raman adiabatic passage is further studied in Publication V, where it is shown that when combined with a Rabi pulse, an arbitrary qutrit state can be prepared.

The problem with adiabatic control is the inherent slowness of the population transfer stemming from the requirement of adiabatic evolution. The shortcuts to adiabaticity can be used to speed up the evolution of the system, or equivalently, to increase the fidelity of an otherwise imperfect adiabatic process. In Publication III we have experimentally demonstrated the validity of the superadiabatic method, where the Hamiltonian governing the time evolution is corrected so that the system follows

exactly its original adiabatic path. In that form, the method has not been previously implemented for STIRAP in any experimental platform and therefore our result significantly contributes to better understanding of adiabatic control. Shortcuts to adiabaticity form an essential bridge between the Rabi methods and adiabatic methods, where the strength of the adiabatic part acts as an interpolation parameter between these two extrema. Understanding the resulting tradeoff between the speed and the robustness is crucial because it can be applied in optimizing the control parameters so that the robustness of the method overcomes the noise from the environment while fast population transfer is still maintained. In Publication I I have shown that a pulse sequence consisting of two fractional STIRAPs can be used to construct a robust superadiabatic NOT-gate. This is an important result, because, as opposed to population transfer between known states, the proposed gate works for an arbitrary initial state, therefore having direct applications in quantum information processing.

The results presented in Publication II are a small detour from the main topic of the thesis, but they are included here due to their interesting practical applications. There we have demonstrated that a superconducting qubit can be used as a Heisenberg-limited sensor for magnetic flux. The result is significant, because already when operating at the standard quantum limit, SQUID loops are among the most sensitive existing magnetic field detectors. The possibility to amplify their sensitivity using a quantum algorithm promises far more accurate detectors in the future.

With the advent of shortcuts to adiabaticity, the robust adiabatic gates investigated here offer a viable alternative to the numerically optimized gate pulses widely used today in circuit QED. The final benefits of robust adiabatic gates are expected to be fully realized only in systems where the internal decoherence rates are no longer the main limiting factor. The opportunities of shortcuts to adiabaticity should be investigated in greater detail in the future, though a clear strength of the adiabatic control is that the origin of the robustness can be theoretically understood.

References

[1] R. P. Poplavskii. Thermodynamic models of information processes. *Usp. Fiz. Nauk*, 115(3):465–501, 1975.

[2] R. S. Ingarden. Quantum information theory. *Reports on Mathematical Physics*, 10(1):43 – 72, 1976.

[3] R. P. Feynman. Simulating physics with computers. *International Journal of Theoretical Physics*, 21(6-7):467–488, 1982.

[4] D. Deutsch. Quantum theory, the church-turing principle and the universal quantum computer. In *Proceedings of the Royal Society of London A: Mathematical, Physical and Engineering Sciences*, volume 400, pages 97–117. The Royal Society, 1985.

[5] D. Deutsch and R. Jozsa. Rapid solution of problems by quantum computation. *Proceedings of the Royal Society of London A: Mathematical, Physical and Engineering Sciences*, 439(1907):553–558, 1992.

[6] L. K. Grover. A fast quantum mechanical algorithm for database search. In *Proceedings of the twenty-eighth annual ACM symposium on Theory of computing*, pages 212–219. ACM, 1996.

[7] P. W. Shor. Algorithms for quantum computation: Discrete logarithms and factoring. In *Foundations of Computer Science, 1994 Proceedings., 35th Annual Symposium on*, pages 124–134. Ieee, 1994.

[8] D. P. DiVincenzo. The physical implementation of quantum computation. *Fortschritte der Physik*, 48(9-11):771–783, 2000.

[9] V. S. Letokhov. Photophysics and photochemistry. *Physics Today*, 30(5):23–32, 1977.

[10] C. Brif, R. Chakrabarti, and H. Rabitz. Control of quantum phenomena: past, present and future. *New Journal of Physics*, 12(7):075008, 2010.

[11] Q. A. Turchette, C. J. Hood, W. Lange, H. Mabuchi, and H. J. Kimble. Measurement of conditional phase shifts for quantum logic. *Phys. Rev. Lett.*, 75:4710–4713, Dec 1995.

[12] R. Schirhagl, K. Chang, M. Loretz, and C. L. Degen. Nitrogen-vacancy centers in diamond: nanoscale sensors for physics and biology. *Annual review of physical chemistry*, 65:83–105, 2014.

[13] R. Blatt and C. F. Roos. Quantum simulations with trapped ions. *Nature Physics*, 8(4):277, 2012.

[14] M. Lewenstein, A. Sanpera, V. Ahufinger, B. Damski, A. Sen(De), and U. Sen. Ultracold atomic gases in optical lattices: mimicking condensed matter physics and beyond. *Advances in Physics*, 56(2):243–379, 2007.

[15] F. A. Zwanenburg, A. S. Dzurak, A. Morello, M. Y. Simmons, L. C. L. Hollenberg, G. Klimeck, S. Rogge, S. N. Coppersmith, and M. A. Eriksson. Silicon quantum electronics. *Rev. Mod. Phys.*, 85:961–1019, Jul 2013.

[16] M. H. Devoret, A. Wallraff, and J. M. Martinis. Superconducting Qubits: A Short Review. *eprint arXiv:cond-mat/0411174*, 2004.

[17] V. Bouchiat, D. Vion, P. Joyez, D. Esteve, and M. H. Devoret. Quantum coherence with a single cooper pair. *Physica Scripta*, 1998(T76):165, 1998.

[18] D. Aharonov and M. Ben-Or. Fault-tolerant quantum computation with constant error. In *Proceedings of the Twenty-ninth Annual ACM Symposium on Theory of Computing*, STOC '97, pages 176–188, New York, NY, USA, 1997. ACM.

[19] A. Y. Kitaev. Fault-tolerant quantum computation by anyons. *Annals of Physics*, 303(1):2–30, 2003.

[20] J. M. Gambetta, J. M. Chow, and M. Steffen. Building logical qubits in a superconducting quantum computing system. *arXiv preprint arXiv:1510.04375*, 2015.

[21] A. Blais, R.-S. Huang, A. Wallraff, S. M. Girvin, and R. Schoelkopf. Cavity quantum electrodynamics for superconducting electrical circuits: An architecture for quantum computation. *Physical Review A*, 69(6):062320, 2004.

[22] E. M. Purcell, H. C. Torrey, and R. V. Pound. Resonance absorption by nuclear magnetic moments in a solid. *Phys. Rev.*, 69:37–38, Jan 1946.

[23] H. Walther, B. T.H. Varcoe, B.-G. Englert, and T. Becker. Cavity quantum electrodynamics. *Reports on Progress in Physics*, 69(5):1325, 2006.

[24] A. Imamoglu, D. D. Awschalom, G. Burkard, D. P. DiVincenzo, D. Loss, M. Sherwin, and A. Small. Quantum information processing using quantum dot spins and cavity qed. *Phys. Rev. Lett.*, 83:4204–4207, Nov 1999.

[25] B. D. Josephson. Possible new effects in superconductive tunnelling. *Physics letters*, 1(7):251–253, 1962.

[26] J. E. Mooij, T. P. Orlando, L. Levitov, Lin Tian, Caspar H. van der Wal, and Seth Lloyd. Josephson persistent-current qubit. *Science*, 285(5430):1036–1039, 1999.

[27] A. Lupaşcu, P. Bertet, E. F. C. Driessen, C. J. P. M. Harmans, and J. E. Mooij. One- and two-photon spectroscopy of a flux qubit coupled to a microscopic defect. *Phys. Rev. B*, 80:172506, Nov 2009.

[28] J. M. Martinis, S. Nam, J. Aumentado, K. M. Lang, and C. Urbina. Decoherence of a superconducting qubit due to bias noise. *Phys. Rev. B*, 67:094510, 2003.

[29] J. M. Martinis, S. Nam, J. Aumentado, and C. Urbina. Rabi oscillations in a large josephson-junction qubit. *Phys. Rev. Lett.*, 89:117901, Aug 2002.

[30] J. Koch, T. M. Yu, J. Gambetta, A. A. Houck, D. I. Schuster, J. Majer, A. Blais, M. H. Devoret, S. M. Girvin, and R. J. Schoelkopf. Charge-insensitive qubit design derived from the cooper pair box. *Phys. Rev. A*, 76:042319, Oct 2007.

[31] Y. Makhlin, G. Schön, and A. Shnirman. Quantum-state engineering with josephson-junction devices. *Rev. Mod. Phys.*, 73:357–400, May 2001.

[32] J. Meixner, F.W. Schäfke, and G. Wolf. *Mathieu Functions and Spheroidal Functions and their Mathematical Foundations: Further Studies*. Lecture Notes in Mathematics. Springer Berlin Heidelberg, 1980.

[33] I. Kovacic and M. J. Brennan. *The Duffing equation: nonlinear oscillators and their behaviour*. John Wiley & Sons, 2011.

[34] J. N. L. Connor, T. Uzer, R. A. Marcus, and A. D. Smith. Eigenvalues of the schrödinger equation for a periodic potential with nonperiodic boundary conditions: A uniform semiclassical analysis. *The Journal of Chemical Physics*, 80(10):5095–5106, 1984.

[35] A. Lupaşcu, S. Saito, T. Picot, P. C. De Groot, C. Harmans, and J. Mooij. Quantum non-demolition measurement of a superconducting two-level system. *Nature Physics*, 3(2):119–125, 2007.

[36] B. Peropadre, P. Forn-Díaz, E. Solano, and J. J. García-Ripoll. Switchable ultrastrong coupling in circuit qed. *Phys. Rev. Lett.*, 105:023601, Jul 2010.

[37] C. Kraglund Andersen and A. Blais. Ultrastrong coupling dynamics with a transmon qubit. *New Journal of Physics*, 19(2):023022, 2017.

[38] R. Bianchetti, S. Filipp, M. Baur, J. M. Fink, C. Lang, L. Steffen, M. Boissonneault, A. Blais, and A. Wallraff. Control and tomography of a three level superconducting artificial atom. *Phys. Rev. Lett.*, 105:223601, Nov 2010.

[39] C. Zener. Non-adiabatic crossing of energy levels. In *Proceedings of the Royal Society of London A: Mathematical, Physical and Engineering Sciences*, volume 137, pages 696–702. The Royal Society, 1932.

[40] M. P. Silveri, K. S. Kumar, J. Tuorila, J. Li, A. Vepsäläinen, E. V. Thuneberg, and G. S. Paraoanu. Stückelberg interference in a superconducting qubit under periodic latching modulation. *New Journal of Physics*, 17(4):043058, 2015.

[41] M. Born and V. Fock. Beweis des adiabatensatzes. *Zeitschrift für Physik*, 51(3):165–180, Mar 1928.

[42] L. I. Schiff. *Quantum Mechanics*. McGraw-Hill, 1949.

[43] N. V. Vitanov, A. A. Rangelov, B. W. Shore, and K. Bergmann. Stimulated raman adiabatic passage in physics, chemistry, and beyond. *Rev. Mod. Phys.*, 89:015006, Mar 2017.

[44] J. Du, L. Hu, Y. Wang, J. Wu, M. Zhao, and D. Suter. Experimental study of the validity of quantitative conditions in the quantum adiabatic theorem. *Physical review letters*, 101(6):060403, 2008.

[45] D. M. Tong, K. Singh, L. C. Kwek, and C. H. Oh. Sufficiency criterion for the validity of the adiabatic approximation. *Physical review letters*, 98(15):150402, 2007.

[46] Y. Aharonov and J. Anandan. Phase change during a cyclic quantum evolution. *Physical Review Letters*, 58(16):1593, 1987.

[47] B. P. Lanyon, M. Barbieri, M. P. Almeida, T. Jennewein, T. C. Ralph, K. J. Resch, G. J. Pryde, J. L. O'Brien, A. Gilchrist, and A. G. White. Simplifying quantum logic using higher-dimensional hilbert spaces. *Nat Phys*, 5(2):134–140, Feb 2009.

[48] U. Gaubatz, P. Rudecki, S. Schiemann, and K. Bergmann. Population transfer between molecular vibrational levels by stimulated Raman scattering with partially overlapping laser fields. a new concept and experimental results. *The Journal of Chemical Physics*, 92:5363–5376, 1990.

[49] J. R. Kuklinski, U. Gaubatz, F. T. Hioe, and K. Bergmann. Adiabatic population transfer in a three-level system driven by delayed laser pulses. *Phys. Rev. A*, 40:6741–6744, Dec 1989.

[50] G. S. Vasilev, A. Kuhn, and N. V. Vitanov. Optimum pulse shapes for stimulated raman adiabatic passage. *Phys. Rev. A*, 80:013417, Jul 2009.

[51] B. T. Torosov and N. V. Vitanov. Composite stimulated raman adiabatic passage. *Phys. Rev. A*, 87:043418, Apr 2013.

[52] N.V. Vitanov and S. Stenholm. Properties of stimulated raman adiabatic passage with intermediate-level detuning. *Optics Communications*, 135(4):394 – 405, 1997.

[53] J. Klein, F. Beil, and T. Halfmann. Robust population transfer by stimulated raman adiabatic passage in a pr^{3+}:$\mathrm{y_2sio_5}$ crystal. *Phys. Rev. Lett.*, 99:113003, Sep 2007.

[54] N. V. Vitanov and S. Stenholm. Analytic properties and effective two-level problems in stimulated raman adiabatic passage. *Phys. Rev. A*, 55:648–660, Jan 1997.

[55] P. Marte, P. Zoller, and J. L. Hall. Coherent atomic mirrors and beam splitters by adiabatic passage in multilevel systems. *Phys. Rev. A*, 44:R4118–R4121, Oct 1991.

[56] N. V. Vitanov, K.-A. Suominen, and B. W. Shore. Creation of coherent atomic superpositions by fractional stimulated Raman adiabatic passage. *Journal of Physics B: Atomic, Molecular and Optical Physics*, 32(18):4535 – 4546, 1999.

[57] M. Weitz, B. C. Young, and S. Chu. Atomic interferometer based on adiabatic population transfer. *Phys. Rev. Lett.*, 73:2563–2566, Nov 1994.

[58] F. Motzoi, J. M. Gambetta, P. Rebentrost, and F. K. Wilhelm. Simple pulses for elimination of leakage in weakly nonlinear qubits. *Phys. Rev. Lett.*, 103:110501, Sep 2009.

[59] M. Demirplak and S. A. Rice. Adiabatic population transfer with control fields. *The Journal of Physical Chemistry A*, 107(46):9937–9945, 2003.

[60] M. V. Berry. Transitionless quantum driving. *Journal of Physics A: Mathematical and Theoretical*, 42(36):365303, 2009.

[61] M. Demirplak and S. A. Rice. On the consistency, extremal, and global properties of counterdiabatic fields. *The Journal of chemical physics*, 129(15):154111, 2008.

[62] M. Demirplak and S. A. Rice. Assisted adiabatic passage revisited. *The Journal of Physical Chemistry B*, 109(14):6838–6844, 2005. PMID: 16851769.

[63] M. G. Bason, M. Viteau, N. Malossi, P. Huillery, E. Arimondo, D. Ciampini, R. Fazio, V. Giovannetti, R. Mannella, and O. Morsch. High-fidelity quantum driving. *Nature Physics*, 8(2):147–152, 2012.

[64] X. Chen, I. Lizuain, A. Ruschhaupt, D. Guéry-Odelin, and J. G. Muga. Shortcut to adiabatic passage in two- and three-level atoms. *Phys. Rev. Lett.*, 105:123003, Sep 2010.

[65] C. H. Bennett, D. P. DiVincenzo, J. A. Smolin, and W. K. Wootters. Mixed-state entanglement and quantum error correction. *Physical Review A*, 54(5):3824, 1996.

[66] L. Giannelli and E. Arimondo. Three-level superadiabatic quantum driving. *Phys. Rev. A*, 89:033419, Mar 2014.

[67] A. Kuhn, G. W. Coulston, G. Z. He, S. Schiemann, K. Bergmann, and W. S. Warren. Population transfer by stimulated raman scattering with delayed pulses using spectrally broad light. *The Journal of chemical physics*, 96(6):4215–4223, 1992.

[68] X. Chen, E. Torrontegui, and J. G. Muga. Lewis-riesenfeld invariants and transitionless quantum driving. *Phys. Rev. A*, 83:062116, Jun 2011.

[69] Y.-X. Du, Z.-T. Liang, Y.-C. Li, X.-X. Yue, Q.-X. Lv, W. Huang, X. Chen, H. Yan, and S.-L. Zhu. Experimental realization of stimulated raman shortcut-to-adiabatic passage with cold atoms. *Nature Communications*, 7:12479, 2016.

[70] A. Baksic, H. Ribeiro, and A. A. Clerk. Speeding up adiabatic quantum state transfer by using dressed states. *Phys. Rev. Lett.*, 116:230503, Jun 2016.

[71] B. B. Zhou, A. Baksic, H. Ribeiro, C. G. Yale, F. J. Heremans, P. C. Jerger, A. Auer, G. Burkard, A. A. Clerk, and D. D. Awschalom. Accelerated quantum control using superadiabatic dynamics in a solid-state lambda system. *Nature Physics*, 13:330–334, 2017.

[72] E. Brion, L. H. Pedersen, and K. Mølmer. Adiabatic elimination in a lambda system. *Journal of Physics A: Mathematical and Theoretical*, 40(5):1033, 2007.

[73] X. Lacour, S. Guérin, N.V. Vitanov, L.P. Yatsenko, and H.R. Jauslin. Implementation of single-qubit quantum gates by adiabatic passage and static laser phases. *Optics Communications*, 264(2):362 – 367, 2006. Quantum Control of Light and Matter.

[74] B. L. Higgins, D. W. Berry, S. D. Bartlett, H. M. Wiseman, and G. J. Pryde. Entanglement-free heisenberg-limited phase estimation. *Nature*, 450(7168):393–396, 2007.

[75] B. M. Escher, R. L. de Matos Filho, and L. Davidovich. General framework for estimating the ultimate precision limit in noisy quantum-enhanced metrology. *Nature Physics*, 7(5):406–411, 2011.

[76] A. Y. Kitaev. Quantum measurements and the abelian stabilizer problem. *arXiv preprint quant-ph/9511026*, 1995.

[77] W. van Dam, G. M. D'Ariano, A. Ekert, C. Macchiavello, and M. Mosca. Optimal quantum circuits for general phase estimation. *Physical review letters*, 98(9):090501, 2007.

[78] G. Puentes, G. Waldherr, P. Neumann, G. Balasubramanian, and J. Wrachtrup. Efficient route to high-bandwidth nanoscale magnetometry using single spins in diamond. *Scientific reports*, 4, 2014.

[79] D. Drung, C. Abmann, J. Beyer, A. Kirste, M. Peters, F. Ruede, and T. Schurig. Highly sensitive and easy-to-use squid sensors. *IEEE Transactions on Applied Superconductivity*, 17(2):699–704, 2007.

[80] N. F. Ramsey. A molecular beam resonance method with separated oscillating fields. *Phys. Rev.*, 78:695–699, Jun 1950.

[81] A. Shnirman, Y. Makhlin, and G. Schön. Noise and decoherence in quantum two-level systems. *Physica Scripta*, 2002(T102):147, 2002.

[82] G. Lindblad. On the generators of quantum dynamical semigroups. *Communications in Mathematical Physics*, 48(2):119–130, 1976.

[83] J. Li, G. S. Paraoanu, K. Cicak, F. Altomare, J. I. Park, R. W. Simmonds, M. A. Sillanpää, and P. J. Hakonen. Decoherence, autler-townes effect, and dark states in two-tone driving of a three-level superconducting system. *Phys. Rev. B*, 84:104527, Sep 2011.

[84] A. A. Houck, J. A. Schreier, B. R. Johnson, J. M. Chow, Jens Koch, J. M. Gambetta, D. I. Schuster, L. Frunzio, M. H. Devoret, S. M. Girvin, and R. J. Schoelkopf. Controlling the spontaneous emission of a superconducting transmon qubit. *Phys. Rev. Lett.*, 101:080502, Aug 2008.

[85] E. M. Purcell, H. C. Torrey, and R. V. Pound. Resonance absorption by nuclear magnetic moments in a solid. *Phys. Rev.*, 69:37–38, Jan 1946.

[86] D. I. Schuster. *Circuit Quantum Electrodynamics*. PhD thesis, Yale University, 2007.

[87] A. Wallraff, D. I. Schuster, A. Blais, L. Frunzio, R.-S. Huang, J. Majer, S. Kumar, S. M. Girvin, and R. J. Schoelkopf. Strong coupling of a single photon to a superconducting qubit using circuit quantum electrodynamics. *Nature*, 431(7005):162–167, Sep 2004.

[88] S. M. Girvin. Circuit qed: Superconducting qubits coupled to microwave photons. *Les Houches, Session XCVI*, pages 117–125, 2011.

[89] S. L. Campbell and C. D. Meyer. *Generalized inverses of linear transformations*. SIAM, 2009.

[90] G. E. Shilov. *Linear Algebra*. Dover Publications, 1977.

[91] Åke Björck. *Numerical methods in matrix computations*. Springer, 2016.

Aalto-DD 84/2018

ISBN 978-952-60-7975-2 (printed)
ISBN 978-952-60-7976-9 (pdf)
ISSN-L 1799-4934
ISSN 1799-4934 (printed)
ISSN 1799-4942 (pdf)

Aalto University
School of Science
Department of Applied Physics
www.aalto.fi

BUSINESS + ECONOMY

ART + DESIGN + ARCHITECTURE

SCIENCE + TECHNOLOGY

CROSSOVER

DOCTORAL DISSERTATIONS